AFRL-AFOSR-VA-TR-2023-0198

Realizing Large-Scale Integrated RF Photonic Signal Processing Systems

Vivek Utgikar
UNIVERSITY OF IDAHO MOSCOW
875 PERIMETER DR
MOSCOW, ID, 83844-0001
US

11/22/2022
Final Technical Report

Air Force Research Laboratory
Air Force Office of Scientific Research
Arlington, Virginia 22203
Air Force Materiel Command

REPORT DOCUMENTATION PAGE

PLEASE DO NOT RETURN YOUR FORM TO THE ABOVE ORGANIZATION.

1. REPORT DATE	2. REPORT TYPE	3. DATES COVERED	
20221122	Final	START DATE 20161115	END DATE 20201114

4. TITLE AND SUBTITLE
Realizing Large-Scale Integrated RF Photonic Signal Processing Systems

5a. CONTRACT NUMBER	5b. GRANT NUMBER	5c. PROGRAM ELEMENT NUMBER
	FA9550-17-1-0076	61102F
5d. PROJECT NUMBER	**5e. TASK NUMBER**	**5f. WORK UNIT NUMBER**

6. AUTHOR(S)
Vivek Utgikar

7. PERFORMING ORGANIZATION NAME(S) AND ADDRESS(ES)
UNIVERSITY OF IDAHO MOSCOW
875 PERIMETER DR
MOSCOW, ID 83844-0001
US

8. PERFORMING ORGANIZATION REPORT NUMBER

9. SPONSORING/MONITORING AGENCY NAME(S) AND ADDRESS(ES)	10. SPONSOR/MONITOR'S ACRONYM(S)	11. SPONSOR/MONITOR'S REPORT NUMBER(S)
Air Force Office of Scientific Research 875 N. Randolph St. Room 3112 Arlington, VA 22203	AFRL/AFOSR RTB1	AFRL-AFOSR-VA-TR-2023-0198

12. DISTRIBUTION/AVAILABILITY STATEMENT
A Distribution Unlimited: PB Public Release

13. SUPPLEMENTARY NOTES

14. ABSTRACT
In this project, we demonstrated several large-scale integration of photonic integrated circuits (PICs), with greater than 100 components, using a design and fabrication flow similar to the conventional CMOS electronic integrated circuits (ICs). The scientific goals of this research were to harness integrated photonics to develop a new wireless radio receiver paradigm that overcomes fundamental limitations associated with existing electronic integrated circuits. The research approach was to first develop a photonic design kit with standard cell libraries, compact models and novel rapid simulation techniqques to enable large scale integration of photonic components in PICs. Next, to process RF signals in optical domain, linearized ring-assisted RF-to-optical modulators were developed. The radio-frequency (RF) modulated output is further processed using a reconfigurable optical filter designed using silicon-based tunable microring structures, while rejecting hostile interfering signals. Adaptive tuning algorithms have been developed and implemented using an electronic backend to adaptive tune a desired filter response. Passive PIC reconfigurability using 2D optical mesh architecture was also investigated.

15. SUBJECT TERMS

16. SECURITY CLASSIFICATION OF:			17. LIMITATION OF ABSTRACT	18. NUMBER OF PAGES
a. REPORT U	b. ABSTRACT U	c. THIS PAGE U	UU	47

19a. NAME OF RESPONSIBLE PERSON	19b. PHONE NUMBER *(Include area code)*
GERNOT POMRENKE	426-8426

YIP: Realizing Large-Scale Integrated RF Photonic Signal Processing Systems

Vishal Saxena

AFOSR Award#	FA9550-17-1-0076
Title	YIP: Realizing Large-Scale Integrated RF Photonic Signal Processing Systems
Program Manager	Dr. Gernot Pomrenke
U. Idaho PI	Prof. Vivek Utgikar Professor of Chemical and Materials Engineering Associate Dean of Research, College of Engineering University of Idaho 875 Perimeter Drive MS 1023 Moscow, ID 83844-1023 Email: vutgikar@uidaho.edu
U. Delaware PI (Former PI)	Prof. Vishal Saxena Associate Professor of Electrical and Computer Engineering University of Delaware 110B DuPont Hall Newark, DE 19716 Email: vsaxena@udel.edu
Report Type	Final Report
Period	11/15/2016–11/14/2020
Keywords	AIM Photonics, Hybrid Optoelectronics, Modulator Linearization, Optical Filters, RF photonic receiver, Ring-assisted Mach Zehnder Modulator, Silicon photonics (SiP), Software-defined Radio.

Abstract

In this project, we demonstrated several large-scale integration of photonic integrated circuits (PICs), with greater than 100 components, using a design and fabrication flow similar to the conventional CMOS electronic integrated circuits (ICs). The scientific goals of this research were to harness integrated photonics to develop a new wireless radio receiver paradigm that overcomes fundamental limitations associated with existing electronic integrated circuits. The research approach was to first develop a photonic design kit with standard cell libraries, compact models and novel rapid simulation techniqques to enable large scale integration of photonic components in PICs. Next, to process RF signals in optical domain, linearized ring-assisted RF-to-optical modulators were developed. The radio-frequency (RF) modulated output is further processed using a reconfigurable optical filter designed using silicon-based tunable microring structures, while rejecting hostile interfering signals. Adaptive tuning algorithms have been developed and implemented using an electronic backend to adaptive tune a desired filter response. Passive PIC reconfigurability

using 2D optical mesh architecture was also investigated. Consequently, the developed architecture synergistically integrates several photonic components with an electronic backend using off-the-shelf components to offer unprecedented frequency agility over 10 GHz range of spectrum. Simulation and experimental results have been disseminated for the developed PIC building blocks for a reconfigurable RF photonic receiver. Further development of demonstrated concepts can result in new ultra-wide bandwidth and rapid dynamic tuning software-defined radios and Radars to meet wide ranging government and defense agency communication standards, and facilitate significantly improved interoperability while at the same time being adaptable to hostile jamming. Research outcomes will empower RF IC researchers by equipping them with a new photonics expertise to take on design challenge of 6G wireless by operating over 10 GHz, or higher, of spectrum to achieve several gigabits per second data rates.

I. Final Report for AFOSR YIP Project: Summary

The three years of this ambitious YIP project were overall a success in achieving several of the planned goals towards investigating large scale photonic integration with >100 components and ∼300 electrical pads, chip tape-outs using silicon photonic foundries and resulted in several current and pending publications. While several challenges were encountered due to the complexities of foundry agreements, photonic chip fabrication and packaging using several commercial vendors, and finally the Covid-19, the PI has realized large-scale optoelectronics system-on-a-chip using the AIM Photonics foundry platform. This report provides an overview of the research objectives addressed and the progress achieved during the four project years. Each of the four major research objectives are discussed in this report. Furthermore, several experimental characterization tasks are still ongoing and their projected goals are discussed.

I-1. Research Objective 1: Develop design kit for RF photonic circuits

PI developed a design kit with standard cell library of photonics components with their compact analytical models, to enable wider adoption of photonics into CMOS integrated circuit design flow. Using these models, the PI developed a methodology to simulate and verify RF photonic circuits.

I-1.1) Task 1A: Develop RF Photonics IC Design Kit Fundamental Question(s) Addressed:

- What is the design flow for complex silicon-based photonic integrated circuits (PICs) for fabrication using an MPW?
- How do we co-design photonic and CMOS electronic circuits and perform co-simulation based verification?

Key Achievements:

1. A photonic PIC design flow was developed that started with schematic design in optical circuit simulation tool (Lumerical Interconnect), then their translation into equivalent circuit in an electronic CAD tool (Cadence Virtuoso), followed by co-simulation with CMOS circuits.

2. Development of a Python based layout cell design scripts for generating photonic cell layout. Later, these designs were translated to KLayout tool. A preliminary layout vs schematic flow was developed to verify PIC layout with optical circuit connectivity. The design rule checks were performed through integration of industry standard Mentor Graphic Calibre's DRC tool. While the flow was successful in large PIC tape-out, the LVS and extraction tools can be developed further in collaboration with foundry and CAD tool providers.

I-1.2) Task 1B: Develop Parameterized Compact Model Fundamental Question(s) Addressed:

- How do we simulate model photonic devices and circuits so that they can be simulated in an electronic design automation tool?

Key Achievements:

1. Verilog-A compact modeling approach was developed for simulating SiP components in an electronic design automation (EDA) environment, i.e. Cadence. The compact models were then used to simulate the Mach-Zehnder and microring modulators, and RF photonic filters used in the project.

2. A novel analytical chirped frequency-sweep based simulation scheme was developed for rapid frequency response simulation of optical filters. This work resulted in a conference paper [1] and a journal article each [2].

I-2. Research Objective 2: Investigate linear RF-to-optical modulators with adaptive calibration

I-2.1) Task 2: Develop a Ring-assisted Mach Zehnder modulator using SiP MPW platform that can be adaptively linearized Fundamental Question(s) Addressed:

- How can a silicon-based Mach-Zehnder modulator be linearized for RF photonic applications? Can it be done without electronic linearization? What are the design trade-offs?
- How to adaptively linearize the designed linear RF-to-optical modulator in presence of imperfections and variations due to process, voltage and temperature (PVT)?

Key Achievements:

1. A ring-assisted Mach Zehnder modulator (RAMZM) was designed and fabricated using multi-project wafer (MPW) processes. The modulator achieves optical domain linearization of the compressive Mach Zehnder response.

2. Automatic linearization algorithms have been developed to calibrate the fabricated silicon-based RAMZMs against process and temperature variations. This work resulted in a conference paper [J2] and a journal article currently under review [60].

I-3. Research Objective 3: Investigate widely tunable optical filters with interference rejection

Task 3: Develop silicon-photonic optical filters for RF filtering applications Fundamental Question(s) Addressed:

- How to realize integrated optical filters using a SiP MPW platform so that it can be used in an RF front-end? What are the limits of SiP technologies in realizing a desired interference rejection, narrow bandwidth (high-selectivity), and tunability?
- How much reconfigurability can be achieved using the components realizable in a SiP MPW platform?

Key Achievements:

1. A fixed topology fourth-order filter based on all-pass decomposition scheme was designed and fabricated using a SiP MPW platforms. Algorithms were adapted/designed to tuned the desired optical filter response, even in the presence of process variations and thermal crosstalk. The PIC is currently being tested and algorithms being optimized for rapid filter tuning and reconfiguration.

2. A mesh-based reconfigurable topology was designed and tapeout on the same SiP chip. A 4×4 square mesh was designed with carefully selected optical taps and phase shifters for calibrating against process and temperature variations. The mesh can fit several filter topologies with arbitrary response. This part of the PIC is to be packaged and will be experimentally characterized and results will be disseminated.

I-4. Research Objective 4: Demonstrate a receiver front-end with adaptive tuning

Task 4: Use developed modulator and optical filters to demonstrate an RF receiver front-end Fundamental Question(s) Addressed:

- What is the RF photonic link tradeoffs (gain, noise figure, linearity and power consumption) when using design linearized modulator and optical-domain RF filtering? Do we need an electronic low-noise amplifier (LNA) for such links and what are the associated linearity tradeoffs?
- What are the suitable algorithms and electronic circuit backend to adaptively tune and calibrate the designed optical filters in the RF front-end?
- How to package the resulting electronic-photonic integrated circuits for system-level characterization?

Key Achievements:

1. Analog optical link based on RAMZM was analyzed and compared with MZM-based links. We showed that the linearized RAMZM-based link provides $18\text{dB/Hz}^{\frac{2}{3}}$ or higher SFDR than its MZM counterpart. Furthermore, the tunable RAMZM that we fabricated, provides a trade-off space between the link Gain, Noise, Linearity performances based upon the rings' optical biasing.

2. Experimental characterization of complex PICs, such as the one designed in this project, require complex electronic backend infrastructure for tuning of PICs and applying RF inputs. A hardware prototyping platform was developed to test the designed PICs with nearly 300 electrical pads. First, a high-speed PC board was designed, then a packaging scheme was developed and accomplished through a commercial vendor. Some of the experimental results are presented in this report and the remaining results will be published in conference and journal papers.

I-5. Challenges

A major challenge during the project was getting the legal agreements signed by the University with SUNY Poly/AIM Photonics to obtain their process design kit (PDK). Former PI Saxena managed to get the PDK agreement signed by UI after over two years into the 3-year project. While a small test chip was done using IMEC at Belgium, design work on the large main chip only started in the third-year of the project (July 2019). As the chip was fabricated and shipped, PI Saxena moved to the University of Delaware where the AIM legal agreements were already in place and transferred his lab. Current PI Utgikar is helping with the project management at UI. The plan

was to test the AIM chip in the fourth extension year as a subcontract to UD, which unfortunately coincided with the onset of Covid-19 pandemic leading to lab shutdowns, personnel challenges, and relative unavailability of vendors used for chip packaging. The chip is being packaged on a specially designed PCB for high-speed and its experimental characterization will be shortly performed at UD. Further results and publications will be communicated to AFOSR by UD PI Saxena.

In terms of technical challenges:

- Linearization of silicon MZ modulators is a challenging problem. While the RAMZI structure investigated in this project provides linearization of the MZ optical transmission nonlinearity, the non-linearity in the pn-junction (phase modulator) still persists limiting the SFDR to 100dB range. There are recent developments using Kerr linearization of phase modulator which can help mitigate this and are being pursued by former PI Saxena's group in their research.
- Another technical challenge was development of phase-modulators in the AIM Photonic's process due to lack of device design examples and process-specific data, as the PIC components in the PDK are black-boxed as IP. PI worked with other collaborators to obtain depletion modulator cells which were tested in the AIM process. This is a limitation of this platform compared to other platforms, such ISIPP50G Active Photonics MPW from IMEC, Belgium.

Peer-Reviewed Publications

[J1] M. J. Shawon and V. Saxena, "Rapid Simulation of Photonic Integrated Circuits Using Verilog-A Compact Models," *IEEE Transactions on Circuits and Systems I: Regular Papers*, vol. 67, no. 10, pp. 3331–3341, 2020.

[J2] J. Shawon, Md. and V. Saxena, "Analysis of RF Photonic Link using SiliconPhotonic Ring-Assisted Mach Zehnder Modulator," in *IEEE Int. Midwest Symposium on Circuits and Systems (MWSCAS)*, 2020.

[J3] R. Wang and V. Saxena, "A CMOS Photonic Optical PAM-4 Transmitter Linearized using Three-Segment Ring Modulator," in *IEEE Int. Midwest Symposium on Circuits and Systems (MWSCAS)*, 2019.

[J4] J. Shawon, Md., R. Wang, and V. Saxena, "Design and Modeling of Silicon Photonic Ring-Based Linearized RF-to-Optical Modulator," in *in the proceedings of IEEE Int. Midwest Symposium on Circuits and Systems (MWSCAS)*, 2018.

[J5] R. Wang, J. Shawon, Md., and V. Saxena, "Design and Compact Modeling of Silicon-Photonic Coupling-Based Ring Modulators for Optical Interconnects," in *IEEE Int. Midwest Symposium on Circuits and Systems (MWSCAS)*, 2018.

Publications Under Peer-Review

[K1] M. J. Shawon and V. Saxena, "Analysis of Trade-offs in RF Photonic Links based on Multi-Bias Tuning of Silicon Photonic Ring-Assisted Mach Zehnder Modulators," *under review in the IEEE Transactions on Circuits and Systems I: Regular Papers*, 2021.

Poster Presentations

[P1] J. Shawon and V. Saxena, "Compact Modeling of Linearized CMOS Photonic Modulators for Millimeter-Wave Wireless," in *NSF mmWave RCN Workshop, Tucson*, 1 2018.

[P2] V. Saxena, "Linearized CMOS Photonic Modulators for Millimeter-Wave Wireless," in *NSF mmWave RCN Workshop, Madison*, July 2017.

[P3] ——, "Hybrid CMOS Photonic Integrated Circuits for Millimeter Wave Communication," in *NSF mmWave RCN Workshop*, July 2016.

I-6. Invited Talks

1. "Sustaining Advances in Integrated Circuits in the post CMOS-Scaling Era," at ECE Dept., University of Delaware, Newark, DE, March 2019.

2. "Sustaining Advances in Integrated Circuits in the post CMOS-Scaling Era," at ECE Colloquium, Case Western Reserve University, Cleveland, OH. 2018.

3. Invited talk at Micron Friday Forum on CMOS Photonics Integrated Circuits, Micron Campus, Boise, Aug 2017.

I-7. Chips Fabricated

1. A test chip using IMEC's ISIPP50G Silicon Photonics process, 5mm^2 area, 2018-2019. Contains microring filters and modulators, and RAMZI test structures. Experimentally characterized.

2. A large PIC using AIM Photonic's Active Photonic process, 25mm^2 area in 2019-2020. Contains RAMZI modulator with adaptive tuning, Programmable optical filters, and a programmable mesh. Currently being packaged and experimentally characterized.

I-8. Personnel Supported

Graduate students:

1. Md Jubayer Shawon, MS from University of Idaho (2019), now a PhD candidate at the University of Delaware.

I-9. Awards Received

1. PI Vishal Saxena received DARPA Young Faculty Award 2019 for his project titled "Silicon Photonic enabled Reconfigurable Optical Analog Processor (SiROAP)"

2. PhD student Md Jubayer Shawon received the prestigious IEEE Solid State Circuits Society (SSCS) 2019 Student Travel Grant to attend International Solid-State Circuits Conference (ISSCC) in San Francisco.

Final Report for AFOSR YIP Project: Details

II. Introduction

This project harnesses silicon-based integrated photonics technology to demonstrate large-scale integrated RF photonic systems. The application we target is a widely reconfigurable wireless receiver which can seamlessly operate in the RF to cm-Wave (DC to 20GHz) frequency bands. The architecture shown in Figure 1 aims to synergistically integrate silicon-on-insulator (SOI) based nanophotonics components with complementary metal oxide semiconductor (CMOS) electronic circuits to enable ultra-wide bandwidth and rapid dynamic reconfiguration radios over a wide frequency range. The project leverages the CMOS-compatible fabrication platform such as the one from AIM Photonics through their multi-project wafer (MPW) fabrication shuttles [3]. The project goals are accomplished by first developing a RF photonic design kit with compact models that allow

design and simulation of hybrid optoelectronic circuits using standard electronic IC design tools. Next, these models are used to develop an RF-to-optical modulator with wideband linearization to convert the received RF spectrum into an optical signal by modulating a CW laser. At the same time, we are developing widely tunable integrated optical filters to process the desired band from the received RF spectrum while rejecting interferers. This is achieved using reconfigurable optical filters to create a desired filter response at a specified center frequency and bandwidth.

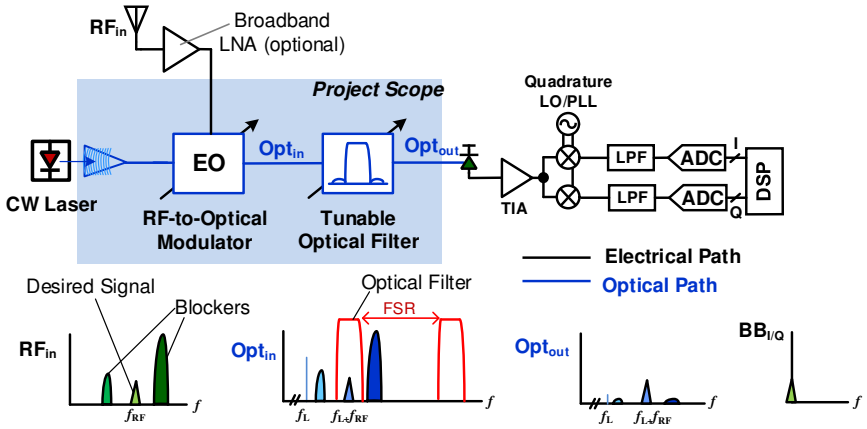

Figure 1: RF-photonic system architecture investigated in this project.

The technical goals of the project are to investigate design and modeling methodology for RF photonic circuits, demonstrate linear RF-to-photonic modulator with >70 dB linearity, widely-tunable optical filters with >40 dB blocker rejection, all integrated in a package; and then use these circuits to demonstrate a wideband RF front-end architecture that is tunable from DC to 10 GHz range with greater than 500MHz RF signal bandwidth.

II-1. MPW Fabrication of Si-based PICs:

Silicon-based electronic-photonic integration is a promising platform for pursuing advances in integrated circuits (IC) in the post-Moore's Law scaling era. As the complementary metal oxide semiconductor (CMOS) technology matures, IC advances are expected from the heterogeneous integration of novel devices such as the silicon-based photonics with standard CMOS or BiCMOS technology. The large instantaneous bandwidth of integrated photonic devices allows enormous data transmission capacity reaching Terabits/s and the optical interconnects realized through on-chip and on-board waveguides and the optical fibers enable low-loss long-distance transmission at such speeds [4].

Silicon-on-insulator (SOI) and Silicon-Nitride (SIN) based ***photonics integrated circuits (PICs)*** are increasingly being used in data center interconnects to achieve higher data rates approaching 100Gbps/wavelength with reduced link energy consumption, compact size, and dramatically lower cost compared to discrete optics or III-V PICs [5]. The increased availability of multi-project wafer (MPW) services such as IME [6], IMEC [7,8] and AIM Photonics [3] are ushering in the Moore's Law equivalent of photonic ICs (where the number of components on a PIC double every two years [9]) by providing fabless PIC fabrication with a design flow similar to the standard CMOS electronic ICs as shown in ***Fig.*** 2). Furthermore, there is a growing amount of activity in RF photonic ICs where the wide tunability and high selectivity of optical filters promise flexible RF front-ends [10,11] and high dynamic range radio-on-fiber links for the next-generation wireless infrastructure [12,13].

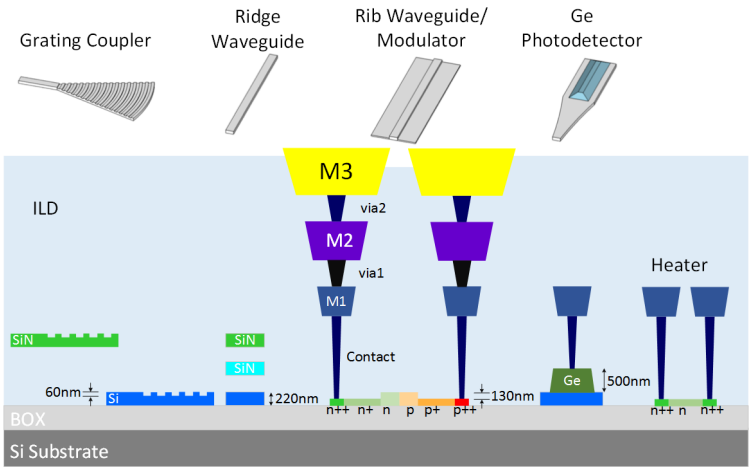

Figure 2: Cross-section showing the layers in a typical silicon photonic fabrication process [3, 5, 8].

III. Research Objective 1: Design Kit and Flow for RF photonic Circuits

III-1. CMOS Photonic IC Design Flow

The ***electronic design automation (EDA)*** tools used for Photonic Integrated Circuit (PIC) design are significantly different from that of Electronic IC design. Additionally, as PIC design is at its early stage of development, no standardized design flow is available to the designers. Moreover, the inter-compatibility between different EDA tools is also a major hurdle in PIC design. Furthermore, to achieve the desired performance of a RF Photonic system, it is mandatory to optimize the design parameters of the optical components according to the application requirements. However, the process design kits (PDKs) provided by the Silicon Photonics foundries only contain static cells of optical components that are not customizable. Therefore, we have developed a complete PIC design flow for CMOS Photonic IC tape-out addressing these challenges.

The design process begins with a simulation tool known as Lumerical Interconnect - a nonlinear transient and scattering data analysis software for PICs [14]. The PIC design is then translated to Cadence schematics employing the Verilog-A based RF Photonic design kit developed by our research group. This allows us to simulate photonic ICs with the interfacing electronic circuits in the same platform. The advantage of such co-design environment is that it allows the designer to simulate complex Electronic-Photonic hybrid systems and perform pre-silicon validation before the chips are sent out for fabrication. Several design iterations are necessary to meet the required specifications.

Once the design is ready, a Python based layout generator IPKISS from Luceda [15], or KLayout [16] is used to create parameterized layout of photonic components. This step has significantly reduced the lead time to design custom photonic components. The layout of the custom components is then imported into an EDA tool (Mentor Graphics Pyxis) or KLayout for Top-level routing. Pyxis and KLayout both allow for waveguide routing with flexible bending radius which is crucial for low loss optical routing. The design rule checks (DRC) are also performed in Pyxis, similar to standard CMOS electronic circuits. The developed PIC design flow is illustrated in ***Fig.*** 3.

III-1.1) Verilog-A Compact Modeling: We have developed a complete design kit with standard cell libraries of components that allow us to design large scale CMOS RF photonic circuits using the same design tools as CMOS electronics. This Verilog-A based design kit completely captures the optical and electrical behavior of the photonic components developed by a Silicon Photonics foundry. As opposed to electrical circuits that only require current/voltage information,

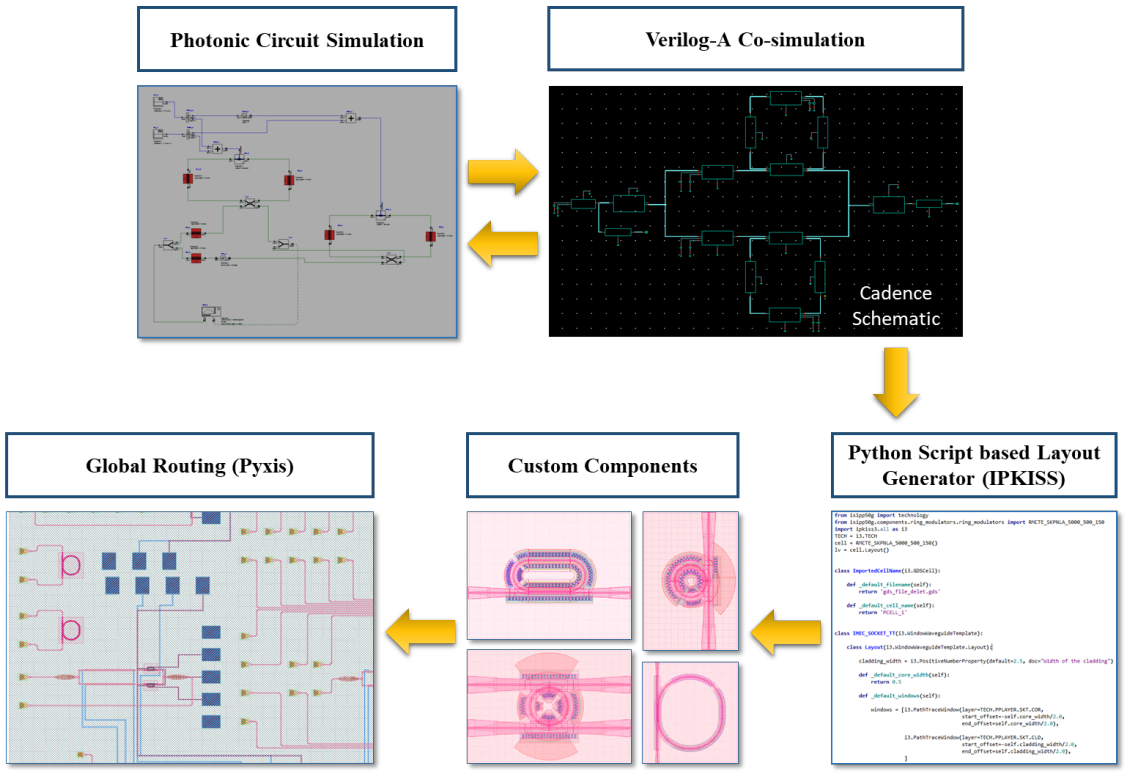

Figure 3: A Photonic Integrated Circuit Design Flow developed for the project.

optical circuits require both electric and magnetic field information as well as their modes and polarizations to fully represent the system. Therefore, in our Verilog-A modeling, light is represented by a complex phasor voltage signal [17]. On the other hand, since light coupled into the ring circulates multiple times inside the ring, there is a transient response that needs to be addressed. Also, the rings are highly wavelength dependent. Since most of our designs contain silicon microrings, we have implemented a wavelength dependent time-domain Verilog-A modeling for most of our library components [17]. Our RF Photonic component library includes Verilog-A model of CW laser, waveguides and bends, splitter, coupler, combiner, thermal phase-shifter, thermo-optic switch, pn-junction phase modulator, Germanium photodetector, optical taps, electro-absorption modulator (IMEC process) and microring modulators. These components are parameterized, thus enhancing design throughput and consistency. ***Fig.*** 3 shows a sample implementation of these components in a Ring Assisted Mach Zehnder Modulator (right) in Cadence environment.

III-1.2) Analytic Modeling: Silicon photonics operates in the mid- and long-wave infrared regions with telecommunications applications being concentrated around the 1330nm and 1550nm laser wavelengths. The latter wavelength translates into $\omega_R = 2\pi \cdot 193\ THz$ center frequency. However, since the signal is obtained by modulating the laser and limited by the electrical bandwidth of the photonic devices (typically <50GHz), only the bandpass spectrum around ω_R is of interest. Thus, similar to carrier modulated communication systems, only the complex baseband equivalent signal and filter response are employed [18, 19]. Here, $\tilde{E}(t)$ is the analytic field which is in turn related to the complex baseband field $E_{bb}(t)$ by

$$\tilde{E}(t) = e^{j\omega_R t} E_{bb}(t) \tag{1}$$

Similar notations are developed for the baseband equivalent of the RF photonic filters:

$$\tilde{h}(t) = e^{j\omega_R t} h_{bb}(t); \quad \tilde{H}(j\omega) = H_{bb}(j(\omega - \omega_R)) \tag{2}$$

Here, $h_{bb}(t)$ is the complex baseband equivalent impulse response of the optical filter, $h(t)$, with respect to the laser carrier frequency. $H_{bb}(j\omega)$ and $H(j\omega)$ are their respective Fourier transforms [20]. Note that these are the baseband equivalent with respect to the laser frequency (ω_R) and not any RF carrier frequency. The input output relationships are now given as [20]

$$E_{out,bb}(t) = \frac{1}{2} h_{bb}(t) * E_{in,bb}(t) \tag{3}$$

Representing the optical signals and filters using their complex baseband significantly relaxes the transient time steps in simulation, i.e. from 1 fs to 10 ps range, which would otherwise be prohibitive to simulate.

Since Verilog-A doesn't natively handle complex arithmetic, real and imaginary signals and filter coefficients are represented as an optical bus $E[0:1]$. The cartesian field is given by $E[0] + jE[1]$ and polar by $E[0]\angle(E[1])$. Without loss of generality, we use electric field magnitude and phase as two Verilog-A 'natures' to represent light in an optical bus. To further simplify the modeling, we only model electric field in forward direction so the backscattering effect is ignored. Therefore, the directional blocks need to be carefully connected with each other. Also, cartesian to polar interconversion, addition and multiplication library blocks are utilized [18, 21].

III-2. Rapid Simulation of RF Photonic Circuits

Design of RF photonic filters requires frequency (or wavelength) sweeps. When using Verilog-A compact model, .ac analysis in Cadence Spectre is challenging as it requires linearization of the component. Therefore, to obtain the frequency response of an optical circuit, prior work employed ***stepped-frequency transient (SFTA)*** simulations [18, 19]. For each frequency point, a transient simulation was performed to obtain the steady-state magnitude and phase response of the system under consideration. SFTA method can be extremely slow, especially when the typical range of frequency sweep is 50 GHz or more to capture the entire ***Free Spectral Range (FSR)*** of ring resonators or filters. The frequency resolution should also be kept sufficiently high, so that the high-Q resonances of such components can be captured with reasonable accuracy. This required improvement in rapid simulation techniques for frequency (or wavelength) sweep without significant loss in frequency resolution.

III-2.1) Broadband Analytic Chirp Excitation: Instead of exciting the system with a frequency tone, a broadband source such as a frequency chirp can be applied to estimate its frequency response in a single transient simulation. A variety of chirps have been used in engineering disciplines to estimate frequency response of a wide range of systems with non-linear dynamics [22–25]. In our context, an analytic chirp stimulation is defined as

$$E_{ch}(t) = E_a(t) \cdot e^{j\varphi(t)} \tag{4}$$

For a simple chirp laser source, $E_a(t) = E_{amp}$ is a constant field magnitude. The phase evolution depends upon the instantaneous frequency, which is swept from a start offset frequency, f_1, to the stop frequency, f_2, over the chirp duration, T, and is expressed as [25]

$$\varphi(t) = 2\pi\Big(f_1 \cdot t + \frac{g \cdot t^{m+1}}{m+1}\Big) \tag{5}$$

where g is a normalizing constant. For $m = 1$, the output is a linear chirp and non-linear for $m > 1$. The frequency can also evolve exponentially (i.e. $f = f_1 b^t$) or logarithmically (for hyperbolic

chirps). For an exponential chirp, $\varphi(t) = 2\pi f_1(\frac{b^t-1}{ln(b)})$, where b is the exponential increase rate [26]. In our compact modeling environment, the laser source model is modified to include a chirped phase. The baseband equivalent linear chirp source is now given by

$$E_{out} = E_{amp}\angle\Big(2\pi \int_0^t (f_1 + g \cdot \tau)d\tau\Big) \tag{6}$$

where $g = \frac{f_2-f_1}{T} = \frac{\Delta F}{T}$, ΔF being the chirp bandwidth.

The baseband equivalent frequency response of the circuit or device under test (DUT) is estimated as

$$H[k] = \frac{X_{out}[k]}{X_{ch}[k]} \tag{7}$$

where X_{ch} are the N_{FFT}-point fast Fourier transform (FFT) of the complex input chirp and X_{out} is the FFT of the complex output of the DUT. Fig. 4 outlines the steps of estimating frequency response of a PIC using chirp signal. In order to satisfy the Nyquist sampling criterion for the entire chirp signal, a sampling rate of $f_s \geq 2f_2$ is required.

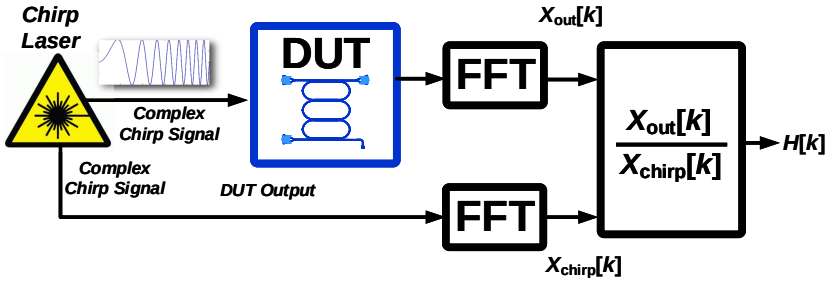

Figure 4: Estimation of frequency response of PIC using our proposed analytic Frequency Chirp Method (FCM).

Fig. 5 illustrates the linear chirp from $f_1 = 10\ GHz$ to $f_2 = 60\ GHz$ with $T = 100\ ns$ generated using the Verilog-A source module. The spectrogram in Fig. 5 (top) shows a linear increase in frequency. Fig. 5 (bottom) illustrates the normalized FFT magnitude response of the complex chirp. The chirp's FFT response exhibits ripples near the edges of desired frequency range (i.e. near f_1 and f_2). The ripples in the complex chirp source appear in the simulated PIC frequency response, $H(k)$, leading to undesirable artifacts and inaccuracies and thus must be minimized.

III-2.2) Time-Bandwidth Product and Fresnel Ripples: In order to understand the source of ripples in the spectrum, Fourier integral of the chirp waveform is considered. Analytical expressions for the linear chirp, essentially a broadband frequency modulation (FM) signal, can be expressed in the form of Fresnel integrals [26, 27]:

$$|X_{ch}(f)| = \sqrt{\frac{T}{2\Delta F}}\Big[(C(x_1) + C(x_2))^2 + (S(x_1) + S(x_2))^2\Big]^{\frac{1}{2}} \tag{8}$$

$$\angle X_{ch}(f) = tan^{-1}\Big(\frac{S(x_1) + S(x_2)}{C(x_1) + C(x_2)}\Big) - 2\pi(f - f_0)^2\frac{T}{2\Delta F} \tag{9}$$

where, $S(x) = \int_0^x sin(\frac{\pi y^2}{2})dy$ and $C(x) = \int_0^x cos(\frac{\pi y^2}{2})dy$ are Fresnel integrals, and $f_0 = \frac{f_1+f_2}{2}$ is the center frequency. The Fresnel arguments x_1 and x_2 are given by

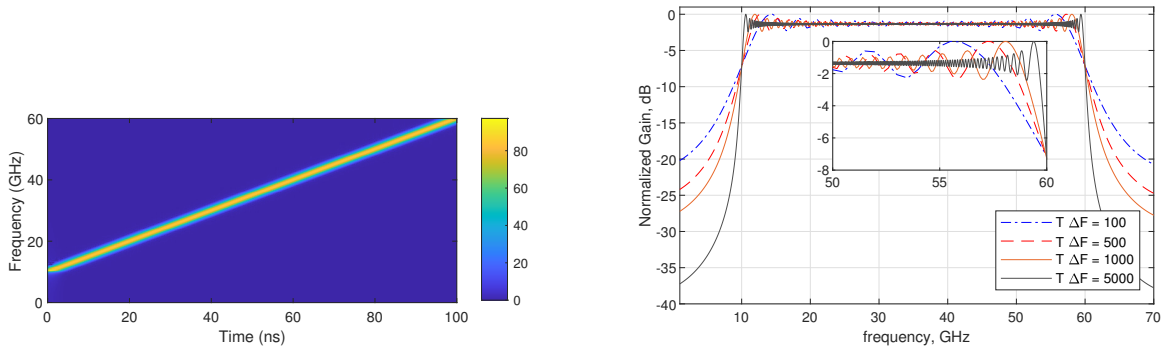

Figure 5: (left) Spectrograph of a linear chirp source with $\Delta F = 50GHz$, $T = 100ns$. (right) Normalized FFT magnitude response of the analytic Chirp source with $T\Delta F = 100, 500, 1000$, and 5000. The inset shows the Fresnel ripples at the right edge of the spectrum (50 to 60 GHz).

$$x_1 = \sqrt{\frac{T \cdot \Delta F}{2}}(1 + r); \quad x_2 = \sqrt{\frac{T \cdot \Delta F}{2}}(1 - r) \tag{10}$$

where $r = 2(\frac{f - f_0}{\Delta F})$ is the scaled frequency. The first term in Eq. 9 approximates to a residual phase of $\frac{\pi}{4}$ over a large frequency range of interest while the second term is the quadratic phase.

From Eqs. 8 - 10, the chirp spectra is a function of the ***time-bandwidth product***, $T \cdot \Delta F$, and independent of center frequency and bandwidth. A lower value of time-bandwidth product results in larger Fresnel ripples in the magnitude spectrum [26]. As seen in Fig. 5 (bottom), with the increase in $T \cdot \Delta F$ from 100 to 5000, the chirp magnitude spectrum gets closer to the ideal rectangular response with flat magnitude and the ripples get less pronounced in the frequency range of interest i.e. between f_1 to f_2. Also, with a larger value of the $T \cdot \Delta F$, phase stays closer to $\frac{\pi}{4}$ in the frequency range of interest [26, 27].

The Fresnel ripples can be pushed to the edge of the desired spectrum by using a large time-bandwidth product. However, these ripples still distort the magnitude spectrum at the edges. The impact of Fresnel ripples can be further mitigated by employing a suitable windowing function such as Tukey, Hann, Blackman-Harris, etc., in the time-domain. The idea is to retain the broadband spectral characteristics of the complex chirp while smoothening the temporal discontinuities at the edges [2].

III-3. RF Photonic Application Circuits

Spectral response of several photonic application circuits have been simulated and verified with an industry standard PIC simulator and with experimental measurements.

III-3.1) CROW Filter: Coupled Resonator Optical Waveguide (CROW) filters are widely used in wavelength division multiplexing (WDM) and are realized by coupling bus waveguides with multiple cascaded optical cavities (microrings) as shown in Fig. 6 (a). In this study, a CROW filter of third order was designed and simulated with the design parameters summarized in Table 1.

This CROW filter is then simulated in our compact modeling framework and analytic FCM. The same filter is also simulated in Lumerical Interconnect - an industry standard photonic integrated circuit simulation tool [28] and with a foundry PDK. Excellent match between the two spectral responses, evaluated in two different simulation platforms, is observed (as shown in Fig. 6) (b). This confirms the accuracy of the compact Verilog-A models of our photonic library components. The same CROW filter is also simulated in Cadence Virtuoso platform employing the SFTA method and

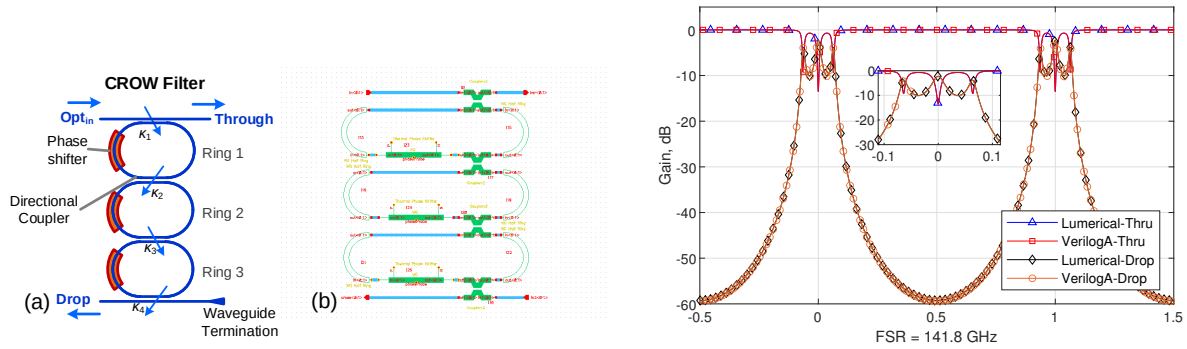

Figure 6: (a) Third-order CROW filter topology, (b) Cadence schematic of the CROW, (c) Estimation of Spectral response of a CROW filter utilizing Lumerical Interconnect and analytic FCM. Here, linear chirp source $\Delta F = 400$GHz and FSR $= 141.8$GHz.

Table 1: CROW Filter Design Parameters

Design Parameter	Value
Ring Circumference (all 3)	500 μm
Coupling coefficients: $[\kappa_1\ \kappa_2\ \kappa_3\ \kappa_4]$	[0.1 0.08 0.08 0.1]

the results are compared in Table 3. The spectral response estimation with a frequency resolution of 1 GHz took 205s to execute using SFTA. In comparison, analytic FCM with $T \cdot \Delta F = 2000$ took only 3.23s for the same frequency resolution and accuracy, which resulted in a 63$\times$ improvement.

III-3.2) APF-based Higher-Order Filters: Here, a PIC with much higher level of complexity is demonstrated. As shown in Fig. 7, an All-Pass-Filter (APF) based optical filter was implemented using ring resonators coupled with the arms of a Mach Zehnder interferometer. To design the filter, all pass decomposition method described in [29] is employed that synthesizes a discrete-time Infinite Impulse Response (IIR) filter into an analog passive ring based structure. First, the filter specifications are translated to a Chebyshev Type-II IIR filter characteristic polynomial. Afterwards, all pass decomposition method is employed to estimate the analog optical filter design parameters, i.e. the coupling coefficients (κ_j), and phase shifts (β and ϕ_j) [30–32]. A sixth-order APF-based filter specifications and design parameters are summarised in Table 2.

Table 2: APF-based Filter Specifications and Design Parameters

APF-based Filter Specifications	**Value**
Filter Order	6
Bandwidth, BW	6.5 GHz
Stopband Attenuation	60 dB
Stopband Edge Frequency	$f_c \pm 8$ GHz
Design Parameter	**Value**
Ring Circumference (all 6)	500 μm
Coupling coefficients: $[\kappa_1\ \kappa_2\ \kappa_3]$	[0.0712 0.3066 0.2056]
Mach Zehnder Arm Phase Shift, β	-1.5723 rad
$[\phi_1 \quad \phi_2 \quad \phi_3]$	[0.1624 0.0579 -0.1356] rad

The spectral response of the filter is then estimated using both Lumerical Interconnect and our simulation framework, utilizing SiP foundry provided data. Again, an excellent match between

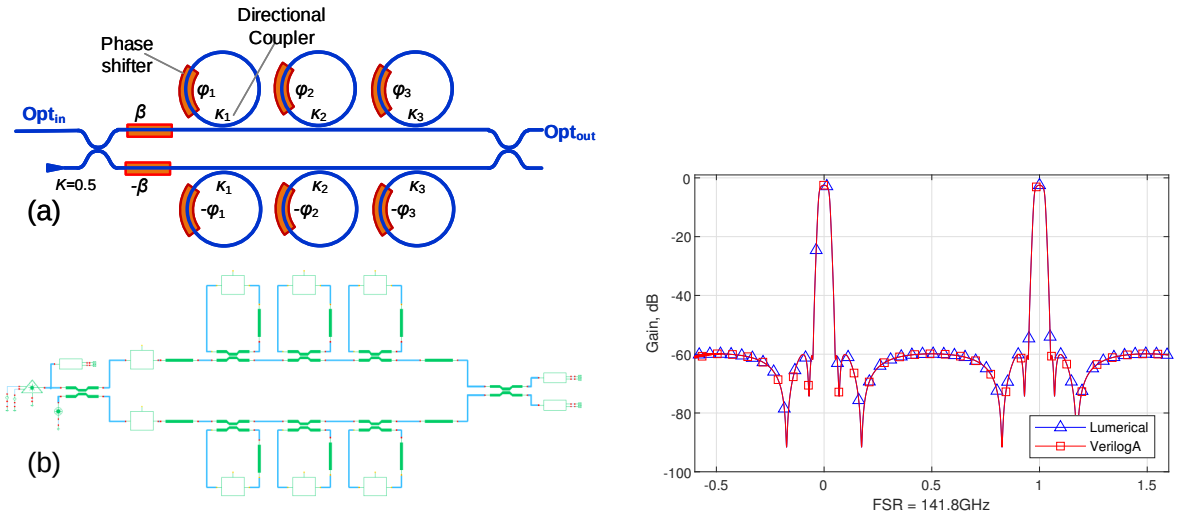

Figure 7: (a) Topology of a sixth-order APF-based filter (b) Cadence schematic of the APF-based Filter, (c) Estimation of Spectral response of a sixth-order APF-based filter utilizing Lumerical Interconnect and analytic FCM. Here, the linear chirp source $\Delta F = 320$GHz and FSR = 141.8GHz

the two spectral responses is observed in Fig. 7 with a 208× speed up in simulation time. Table 3 compares the developed analytic FCM method with prior methods. Here, FCM method took significantly less time, compared to SFTA, to estimate the spectral response of the PICs for the same accuracy and frequency resolution. The analytic FCM method becomes even more advantageous when spectral estimation with high frequency resolution, f_{res}, is required. Also, when the frequency range of interest (ΔF) is very wide, our method offers orders of magnitude improvement in computation time.

Table 3: Performance Comparison

Design	ΔF	f_{res}	SFTA	FCM	MSE	Improv.
CROW	400GHz	1GHz	205s	3.23s	0.12	63×
APF6	320GHz	1GHz	1499.1s	7.21s	0.46	208×
APF6	320GHz	0.1GHz	17215s	17.06s	0.13	1009×
Ring	2.2THz	1GHz	1552s	11.44s	0.015	135×
Vernier	2.2THz	1GHz	8350s	20.84s	0.06	400×

III-3.3) Microring Modulators: A ***microring modulator (MRM)*** shown in ***Fig.*** 8 can be modeled either using its components similar to the ring resonator (i.e. composite model) in the previous section, or using lumped modeling. Lumped modeling is better suited for fitting experimentally measured response of an MRM to its compact model [33–35].

The modulator ring has the resonant frequency $\omega_0 = \frac{2\pi mc}{nL} = \frac{mc}{nR}$, which in our analytic framework, can be substituted by $\omega_0 \rightarrow \omega_0 - \omega_R$. The resonator amplitude decays with a net time-constant τ due to the various losses. The net amplitude delay time constant is contributed by the net losses in the ring (τ_l) and the power coupled to the bus (τ_c) and given by

$$\frac{1}{\tau} = \frac{1}{\tau_c} + \frac{1}{\tau_l} \tag{11}$$

The energy amplitude in a single-bus ring, $a(t)$, is described by the differential equation [35]

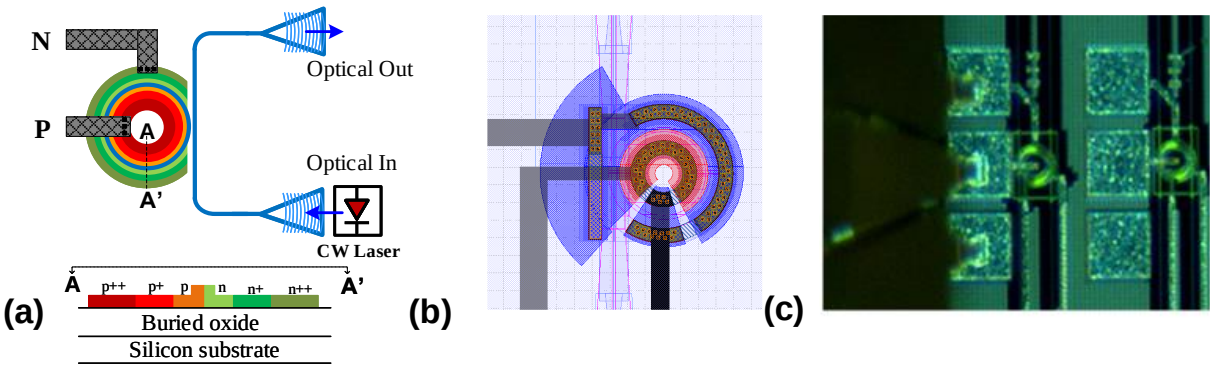

Figure 8: (a) Microring modulator in a SiP process, (b) layout, (c) chip micrograph.

$$\frac{da(t)}{dt} = \Big(j\omega_0 - \frac{1}{\tau_l(t)} - \frac{1}{\tau_c(t)}\Big)a(t) - j\mu E_{in} \tag{12}$$

$$E_{out}(t) = E_{in} - j\mu a(t) \tag{13}$$

Here, $E_{in} = E_0 e^{j\omega_L t}$ in the input wave amplitude, which is typically a CW laser with analytic wavelength, ω_L. E_{out} is the output or thru wave amplitude. The energy cross-coupling factor (μ) relates to the power coupling coefficient (κ^2) and time-constant (τ_c) as [35]

$$\mu^2 = \frac{\kappa^2 v_g}{2\pi R} = \frac{2}{\tau_c} \tag{14}$$

where v_g is the group velocity and R is the ring radius [35].

Solving Eq. 12 for steady-state zero-bias condition, $\tau_l(t) = \tau_l$ and $\tau_c(t) = \tau_c$, and input $E_{in} = E_0 e^{j\omega t}$, we obtain the energy amplitude

$$a = \frac{-j\sqrt{\frac{2}{\tau_c}}}{j(\omega - \omega_0) + \frac{1}{\tau}} E_{in} \tag{15}$$

Substituting this into Eq. 13, we obtain the steady-state field transmission

$$\begin{aligned} \frac{E_{out}}{E_{in}} &= \frac{j(\omega - \omega_0) + \frac{1}{\tau} - \frac{2}{\tau_c}}{j(\omega - \omega_0) + \frac{1}{\tau}} \\ &= \frac{j(\omega - \omega_0) + \frac{1}{\tau_l} - \frac{1}{\tau_c}}{j(\omega - \omega_0) + \frac{1}{\tau_l} + \frac{1}{\tau_c}} \end{aligned} \tag{16}$$

and thus the power transmission is

$$T = \left| \frac{j(\omega - \omega_0) + \frac{1}{\tau_l} - \frac{1}{\tau_c}}{j(\omega - \omega_0) + \frac{1}{\tau_l} + \frac{1}{\tau_c}} \right|^2 \tag{17}$$

This can be interpreted as change in effective index $n(v_m)$ and input-dependence of the time-constants $\tau_l(v_m)$ and $\tau_c(v_m)$.

The differential equation in Eq. 12 is implemented in the Verilog-A model using analytic modeling approach. Here, a reference frequency correspondng to a reference wavelength is used to offset the frequencies of interest. The resulting offset frequency, $\Delta f = c(\frac{1}{\lambda_L} - \frac{1}{\lambda_R})$, is used to excite the laser and is kept in the range under 10-50GHz to speed up simulations. Also, since Verilog-A doesn't

support complex variables, the variables are realized using coupled equations in real variables as shown in Eq. 18 below. The input is $E_{in} = E_{ix} + jE_{iy}$, transmitted wave is $E_{out} = E_{ox} + jE_{oy}$, and the ring energy variable is $a = a_x + ja_y$.

$$\frac{da_x(t)}{dt} = -\omega_0 a_y - \frac{a_x}{\tau(t)} + \mu E_{iy} \tag{18}$$

$$\frac{da_y(t)}{dt} = +\omega_0 a_x - \frac{a_y}{\tau(t)} - \mu E_{ix} \tag{19}$$

Also, the output fields

$$E_{ox} = E_{ix} + \mu a_y \tag{20}$$

$$E_{oy} = E_{iy} - \mu a_a \tag{21}$$

Static Spectral Response: Fig. 9(a) shows the static spectral response of the MRM. A similar set of responses can be easily obtained experimentally from the MRM. Then this data is used to fit the time-constants to the input reverse-bias voltage [33]

$$\Delta\tau_c(v) = \tau_{c0} + \tau_{c1}v + \tau_{c2}v^2 + \cdots \tag{22}$$

$$\Delta\tau_l(v) = \tau_{l0} + \tau_{l1}v + \tau_{cl}v^2 + \cdots \tag{23}$$

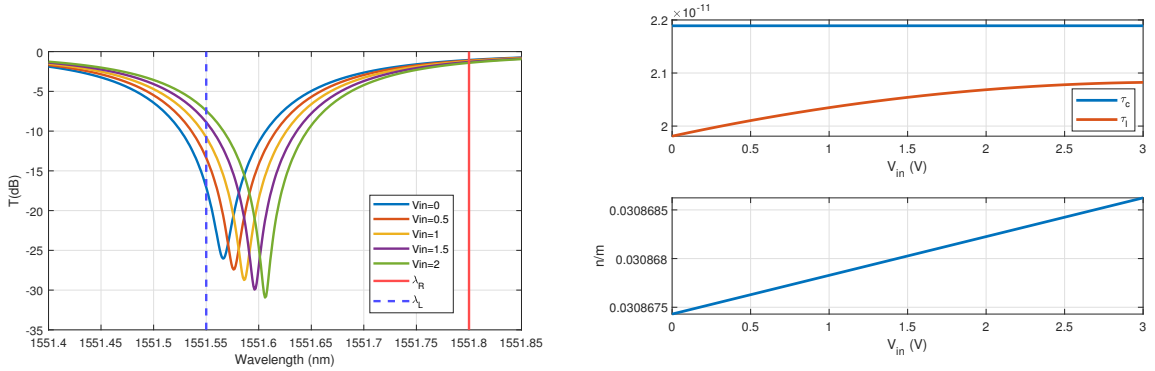

Figure 9: Static transmission response of a microring modulator with wavelength on the x-axis (Matlab generated). Here, the laser input is applied at λ_L =1551.55nm to obtain optical modulation. Also, note that a higher reference wavelength of λ_R =1551.8nm is arbitrarily chosen as a reference for analytic modeling. The resonance is red-shifted (to higher red wavelengths) as the ring is reversed biased. Fitted τ_c, τ_l and $\frac{n}{m}$ parameters with respect to the applied voltage from the experimental static characterization data of an MRM.

Also, the extracted effective index to mode number (m) ratio $\frac{n(v)}{m} = \frac{\lambda_0}{L} = \frac{2\pi c}{\omega_0 L}$ is curve fitted to the voltage as

$$\frac{n(v)}{m} = n_{m0} + n_{m1}v + n_{m2}v^2 + \cdots \tag{24}$$

Fig. 9(b) shows the curve fitted paramaters of the microring modulator [33]. We can observe that as the rind is depleted by applying a higher reverse-bias, V_{in}, the resonance is red-shifted due to the increase in effective index, n. Also, since the optical losses are reduced due to lower free carrier concentration, the quality factor of the detuned rings progressively increases. The electrical behavior of the ring is modeled by including the parastic capacitances and resistances as shown in Fig. 10. The passive network is extracted from s_{11} data using a VNA setup [33] . The depletion capacitance can be made voltage-dependent if it can be accurately extracted.

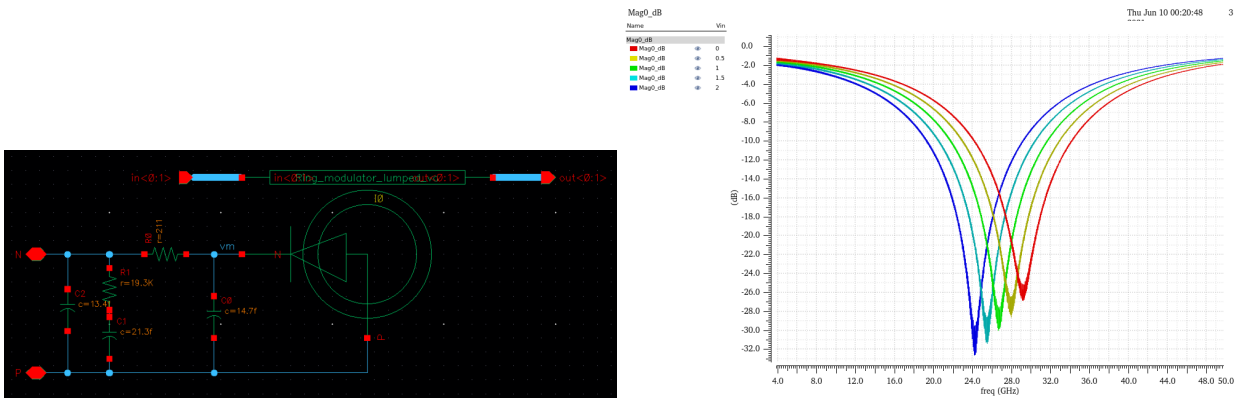

Figure 10: (a) Compact model of the MRM showing the electrical parasitics. The optical model behavior is performed using the Verilog-A code. (b) Simulated static transmission response of a 8μm radius microring modulator using the analytic chirp method with Cadence Spectre. An offset frequency ($\Delta f = f - f_R$) is used on the x-axis, where, $f_R = \frac{c}{\lambda_R}$ and λ_R =1551.8nm, similar to Fig. 9.

Dynamic Transient Response: The ring compact model is now driven with a 28Gbps PRBS-31 pattern with 2.4V peak-to-peak NRZ input. The initial transience during few cycles before the ring reaches its steady-state response are discarded. As shown in Fig. 11, the ring dynamics and this the resulting eye patterns depend upon the optical biasing of the ring. Here, we change the wavelength of the input laser to 1551.45nm, 1551.50nm and 1551.55nm respectively to bias the MRM relative to its resonant wavelength. We can observe in Fig. 11 that the optical biasing of the ring sets the trade-off between the extinction ratio, insertion loss and eye opening.

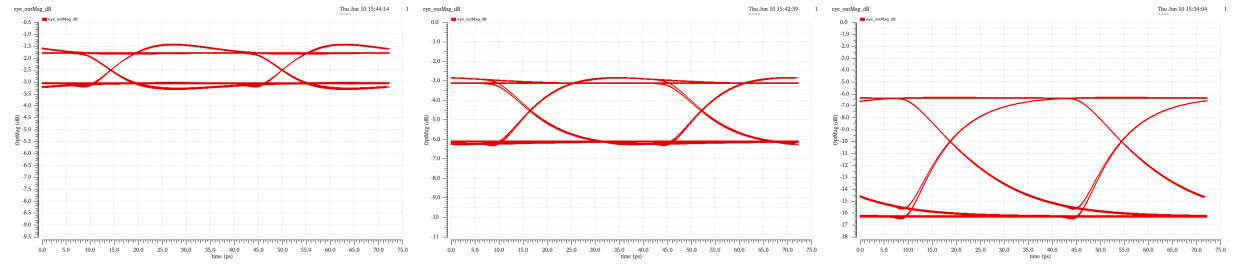

Figure 11: Eye pattern of the MRM optical output when its driven by a 28Gbps PRBS-31 data pattern with 2.4V$_{pp}$ drive. The eye patterns are shown for laser wavelengths 1551.45nm, 1551.50nm and 1551.55nm respectively. Again, here λ_R =1551.8nm.

IV. Research Objective 2: Linearized RF-to-Optical Modulators

IV-1. Linearization of MZ Modulators

A linear RF-to-optical modulation is required before optical-domain signal processing of the radio signal can be performed. Discrete lithium niobate ($LiNbO_3$) MZMs have been widely used in analog photonic links and are limited to < 95 dB/Hz$^{2/3}$ spur-free dynamic range (SFDR) at 1GHz. Linearization of MZMs has been a long-studied topic in RF photonics [36,37] and has recently received renewed interest with the advent of silicon-based MZMs. Several techniques have been explored to linearize an MZM whose linearity is fundamentally limited by the ***compressive*** raised cosine nonlinearity (or sinusoidal nonlinearity around the quadrature bias) with its optical transmission given by

$$T = \frac{T_{ff}}{2}\Big(1 + cos\Big(\frac{\pi v_M}{V_\pi}\Big)\Big) \tag{25}$$
$$= \frac{T_{ff}}{2}\Big(1 - sin\Big(\frac{\pi v_m sin(\omega t)}{V_\pi}\Big)\Big)$$

Here, $T_{ff} = \frac{1}{L}$ is modulator's fiber-to-fiber optical insertion loss, and $V_\pi = V_\pi(f)$ is the modulator voltage to obtain an optical phase shift of π. Also, $v_M = V_{bias,M} + v_m sin(\omega t)$, is the applied voltage where $V_{bias,M}$ is the bias voltage and commonly set to the quadrature transmission point $V_\pi/2$. Assuming perfectly differential drive, we can express the compressive nonlinearity as $T(v) \approx a_0 + a_1 v + a_3 v^3 + O(v^5)$, with $a_1 a_3 < 0$. Linearization of a silicon-based MZM is especially challenging due to the electrical nonlinearities incurred in the nonlinear C-V response of the reverse-biased pn-junction and the nonlinear relationship between optical phase shift and the voltage applied across the pn-junction [38].

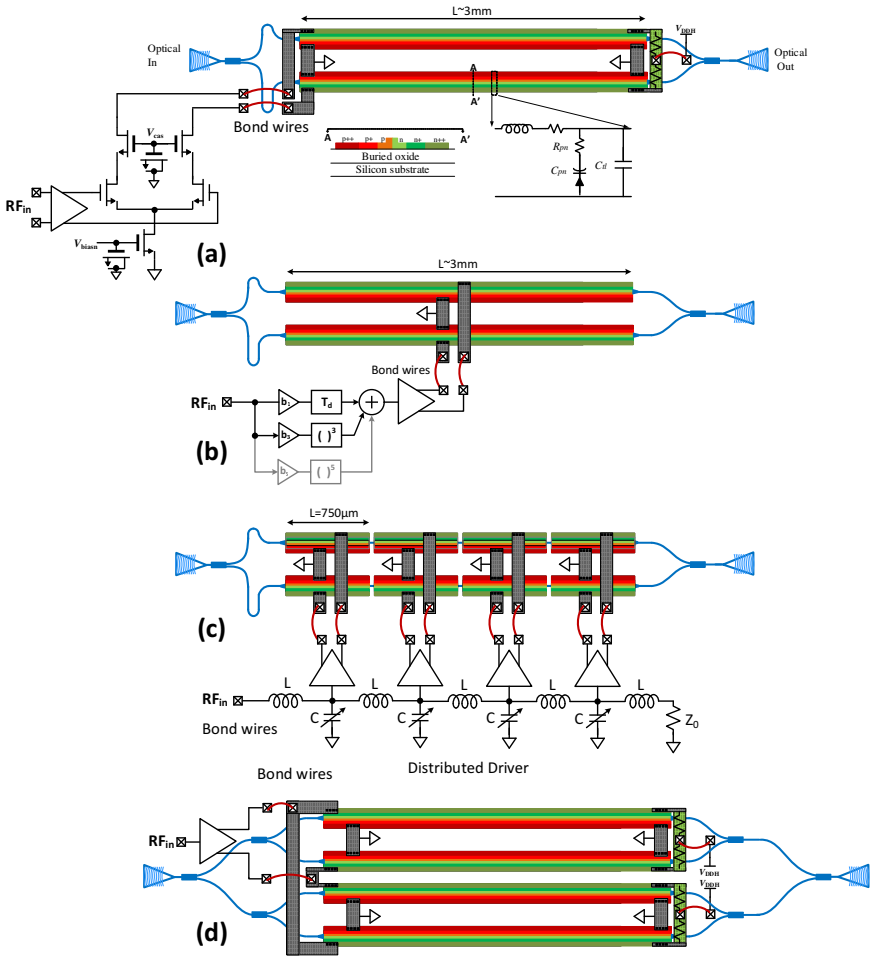

Figure 12: **MZM Linearization:** (a) A traveling-wave electrode Mach-Zehnder modulator (MZM) with current-mode driver circuit for NRZ waveforms. The modulator arms are typically $\geq$ 3mm long and designed using depletion-mode pn junctions. The MZM exhibits a compressive odd-order nonlinearity in its EO response. (b) A pre-distortion driver can be designed to compensate for the MZM EO response. Typical realizations have used lumped driver which results in low EO bandwidth. (c) The MZM arms can be segmented to realize a distributed drive topology. A distributed amplifier is realized by creating an artificial TLine of CMOS/BiCMOS amplifiers. (d) A Dual-Parallel MZM can also be used to linearize the EO response with a larger PIC layout footprint.

IV-1.1) Traveling-wave MZM: A silicon-based MZM is realized using phase shifter arms with depletion-mode pn-junctions as shown in ***Fig.*** 12(a). In order to optimize the insertion loss and optical phase shift produced, low-doped pn-junctions are employed which are typically ∼3-4mm. A traveling-wave drive allows wide electro-optic (EO) bandwidth by absorbing the capacitance of the phase shifter in an on-chip transmission line (TLine) achieving > 35GHz bandwidth in SiP platforms [3]. A traveling-wave MZM is driven using a current-mode CMOS/BiCMOS differential driver that allows a large voltage swing while allowing impedance matching with the MZM TLine [39, 40]. Silicon-based analog MZMs have been designed where DC Kerr non-linearity was used to compensate for the pn-junction non-linearity to achieve a broadband SFDR linearity of ∼ 106 dB/Hz$^{2/3}$ over a 13GHz bandwidth [41, 42]. However, for long MZM length, the sinusoidal MZ nonlinearity still persists.

Active electronic linearization of $LiNbO_3$ and SiP MZMs using a CMOS pre-distortion circuit has been investigated using third or fifth-order active pre-distortion [43, 44] as shown in Fig. ***Fig.*** 12(b). The idea here is to create an ***expansive*** voltage transfer characteristic, $g(v) = T^{-1}(v) = b_1v + b_3v^3$, with $b_1b_3 > 0$ to compensate for the compressive transmission of the MZM so that $T(g(v)) \approx a_0 + a_1b_1v$. However, the literature has demonstrated only lumped driven MZM with third and/or fifth-order nonlinearity cancellation as shown in ***Fig.*** 12(b). Moreover, the analog predistortion blocks used complex circuitry without any consideration for the resulting noise figure. Due to the lumped drive, the active linearization techniques exhibit lower bandwidths (< 1.05GHz), and incur noise penalty and supply voltage limitations (Bi/CMOS supply voltage).

IV-1.2) Distributed MZM Driver: Distributed MZM drivers segment the MZM arms into several lumped segments of $500 - 700\mu m$ each which are then driven by a distributed CMOS or BiCMOS amplifier as shown in ***Fig.*** 12(c) [45, 46]. The optical and electrical group velocities are matched using on-chip tuning of delays. The distributed driver allows broadband drive of the MZM. Driving the nonlinear capacitance of depletion-mode pn-junction using a low drive resistance reduces the impact of the nonlinearity placing the MZM in the $101 - 109$ dB/Hz$^{2/3}$ SFDR range in the 1-20 GHz frequency range [38]. Further linearization is needed to realize higher SFDR by compensating for the MZ optical nonlinearity. A third-order intermodulation (IM_3) cancellation technique using second-order intermodulation (IM_2) injection was recently demonstrated with 120 dB/Hz$^{2/3}$ SFDR at 9GHz [38]. However, IM_2 injection is fundamentally a narrowband technique and likely to work only when the two-tone signals, used for SFDR measurements, are spaced closed together [47].

IV-1.3) Dual Parallel MZMs: Dual parallel MZMs as shown in ***Fig.*** 12(d) can also be used to linearize MZM response at the cost of higher PIC complexity and tuning knobs needed for tuning any process and temperature induced mismatch [48].

IV-1.4) Microring Modulators: Microring modulators (MRM) allow modulation with a very small form-factor ($\sim 5\mu m$ radius) and lumped capacitive interface, but typically suffer both even as well as odd-order distortion due to the Lorentzian optical transmission of the microring. Consequently, SiP MRMs exhibit an SFDR of 63 dB/Hz$^{2/3}$ with single-ended drive [49]. Linearization of MRMs has been attempted but the resulting performance is limited below 98 dB/Hz$^{2/3}$ up to 13 GHz [12].

IV-2. Ring-assisted Mach Zehnder Modulator

In the last decade, linearized ***Ring-assisted MZ Modulators (RAMZM)*** have been explored where a differential configuration, similar to the MZM, is employed but the two (upper and lower) phase shifters are replaced by ring modulators as shown in Fig. 13. By exploiting the Lorentzian transmission characteristics, upper and lower rings can be optically biased such that their voltage-to-phase

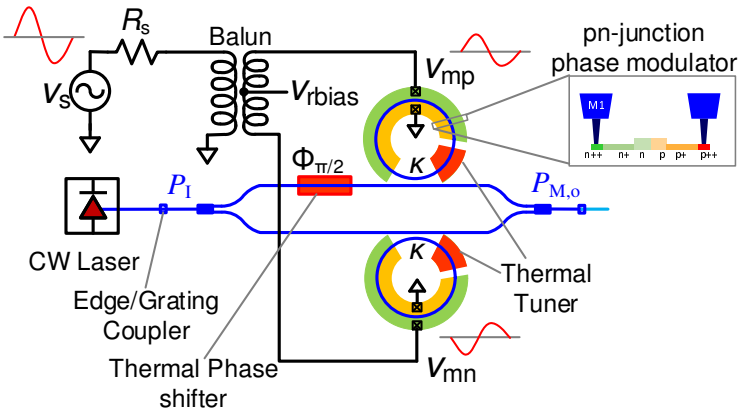

Figure 13: Conceptual schematic of a silicon photonic Ring Assisted Mach Zehnder Modulator (RAMZM), interfaced with an RF source and a CW laser source.

transfer characteristic is expansive; this property is used to realize optical-domain pre-distortion. This expansive response can be enhanced by a suitable value of coupling coefficient (κ) and then used to compensate for the compressive phase-to-intensity non-linearity of a Mach-Zehnder interferometer [11,50–52]. The MZ push-pull configuration suppresses and even-order non-linearity, similar to an MZM. Fig. 13 shows the schematic of a SiP RAMZM and its interface with the RF input source using a differential balun. Fig. 14 shows the chip micrograph of an RAMZM fabricated using IMEC's ISIPP50G SiP process [8]. As shown in Fig. 13, the output of the CW laser is equally split into two arms of the MZM. RF signals are applied to the ring modulators in a differential push-pull configuration around a DC bias (V_M). These differential RF signals are translated into different phase changes in each arms of the MZI. When the two optical fields combine at the output of the MZM, optical modulation is achieved via constructive or destructive interference [4].

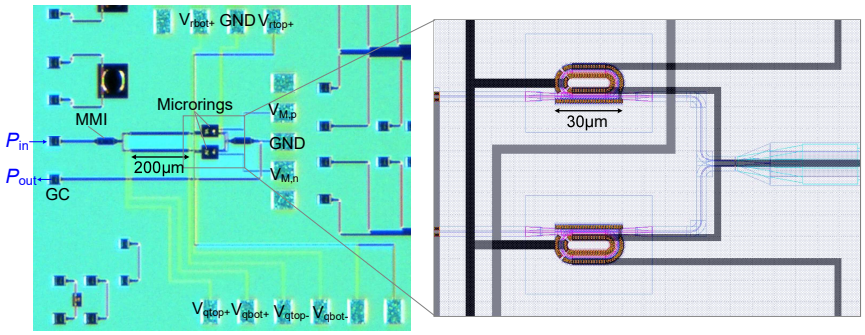

Figure 14: Chip micrograph of a RAMZM fabricated in IMEC's ISIPP50G SiP process.

IV-2.1) RAMZM Transmission Characteristics: We now show the transmission characteristics of the RAMZM. The optical wave electric field at the output of a RAMZM can be expressed as [53]

$$E_{out} = \frac{E_{in}}{2}\Big(|a_{r1}(\theta)|\, e^{-j.(knL_1+\phi_{bias}+\angle a_{r1}(\theta))} + \cdots + |a_{r2}(\theta)|\, e^{-j.(knL_2+\angle a_{r2}(\theta))}\Big) \tag{26}$$

$$a_{ri}(\theta) = \frac{\tau - \alpha e^{-j\theta}}{1 - \tau\alpha e^{-j\theta}} \tag{27}$$

where the variables are defined below. Here, index term $i = 1$ refers to upper while $i = 2$ refers to the lower arm of RAMZM.
E_{in}: input electric field
L_i: length of the RAMZM arms
$|a_{ri}(\theta)|$: microring magnitude response
$\angle a_{ri}(\theta)$: microring phase response
ϕ_{bias}: phase difference between the upper and lower arms introduced by thermal phase shifter
$\tau = \sqrt{1-\kappa^2}$: transmission coefficient of the microring couplers
α: microring loss factor
$\theta = \theta(V)$: microring roundtrip phase shift, which depends on the applied voltage in the phase-modulators.
If we neglect losses in the short MZI arms, the transmission function, $T(\theta) = \frac{I_{out}}{I_{in}} = \left|\frac{E_{out}}{E_{in}}\right|^2$, can be written as

$$T(\theta) = \frac{1}{4}\left|e^{-j.(knL_1+\phi_{bias}+\angle a_{r1}(\theta))} + e^{-j.(knL_2+\angle a_{r2}(\theta))}\right|^2 \tag{28}$$

When the optical path of the RAMZM arms have equal length ($L_2 = L_1$), the transfer function can be simplified as

$$T(\theta) = \frac{1}{2}\left[1 + \cos\left(\phi_{bias} + \angle a_{r1}(\theta) - \angle a_{r2}(\theta)\right)\right] \tag{29}$$

$$\phi_i = \angle a_{ri}(\theta) = \tan^{-1}\left(\frac{\alpha(1-\tau^2)\sin\theta}{\tau(1+\alpha^2) - \alpha(1+\tau^2)\cos\theta}\right) \tag{30}$$

As mentioned earlier, θ is the round-trip phase delay in the microrings. By applying differential signal ($\theta = \theta_{DC} \pm \theta_{mod}$) in the microrings, one can achieve electro-optic modulation. Here, θ_{DC} is the microring optical DC bias point, whereas θ_{mod} is the modulating RF input signal. Now, if we assume low-loss rings, i.e. $\alpha \approx 1$, and apply differential modulating signal, trigonometric manipulation of $T(\theta)$ and expanding its series around θ_{mod} gives us Eqs. 31 to 36 [36, 54].

$$P_{M,o}(\theta_{mod}) = P_I T(\theta) = \frac{P_I\gamma_0}{2} - \gamma_1 P_I\theta_{mod} - \gamma_2 P_I\theta_{mod}^2 + \gamma_3 P_I\theta_{mod}^3 + \gamma_4 P_I\theta_{mod}^4 + \mathcal{O}(\theta_{mod}^5) \tag{31}$$

$$\gamma_0 = 1 + \cos(\phi_{bias}) \tag{32}$$

$$\gamma_1 = \frac{(\tau^2-1)\cdot\sin(\phi_{bias})}{\tau^2 - 2\tau\cos(\theta_{DC}) + 1} \tag{33}$$

$$\gamma_2 = \frac{(\tau^2-1)^2\cdot\cos(\phi_{bias})}{(\tau^2 - 2\tau\cos(\theta_{DC}) + 1)^2} \tag{34}$$

$$\gamma_3 = \frac{(\tau^2-1)[2\cos^2(\theta_{DC})\tau^2 + \cos(\theta_{DC})\tau^3 + 2\tau^4 + \cos(\theta_{DC})\tau - 8\tau^2 + 2]\cdot\sin(\phi_{bias})}{3(\tau^2 - 2\tau\cos(\theta_{DC}) + 1)^3} \tag{35}$$

$$\gamma_4 = \frac{(\tau^2-1)^2[4\cos^2(\theta_{DC})\tau^2 + 2\cos(\theta_{DC})\tau^3 + \tau^4 + 2\cos(\theta_{DC})\tau - 10\tau^2 + 1]\cdot\cos(\phi_{bias})}{(\tau^2 - 2\tau\cos(\theta_{DC}) + 1)^4} \tag{36}$$

In these equations, P_I is the modulator optical input power. Upon observing Eqs. 31–36, we can observe that even-order distortions can entirely be eliminated simply by setting $\phi_{bias} = \frac{\pi}{2}$. This is achieved by tuning thermal heaters on the RAMZM arms [4]. On the other hand, the third-order nonlinearity can be canceled by setting the rings at the anti-resonance point (i.e. optical bias $\theta_{DC} = \pi$) [51]. This is achieved by tuning the thermal phase shifters of the microrings while the driver voltage is set to the common-mode voltage, V_M DC. The differential modulating signals, v_m, are applied around this common-mode voltage, so that the individual ring drive voltages are $V_M \pm v_m$. Therefore, the round-trip phase shift at the upper and lower ring will be $\pi + \theta_{mod}(v_m)$ and $\pi - \theta_{mod}(v_m)$, respectively.

IV-2.2) RAMZM Optical Biasing: As mentioned before, biasing schemes are implemented on a SiP RAMZM by means of thermal phase shifters as seen earlier in Fig. 14. This chip was fabricated in IMEC's ISIPP50G SiP process. Here, smaller ring size was employed with a fixed coupling ratio (κ). The SiP RAMZM presented in this work utilizes n-doped resistive heaters [55] placed around the arms and rings to tune ϕ_{bias} (arm bias) and θ_{DC} (ring bias), respectively. The change in spectral response of the RAMZM with various arm bias voltages (0-14V DC) is shown in Fig. 15. Here, a laser source was coupled into the on-chip RAMZM by means of a 4-channel fiber array through a grating coupler [4]. The RAMZM output was taken off the chip via another grating coupler and fiber array channel. The other end of the latter fiber array channel was terminated at a Keysight N7744A photodetector.

Similarly, by applying 0-7V DC on the ring heaters, the resonances of the lower (Fig. 15(left)) and upper (Fig. 15(right)) ring were tuned. Here, it can be seen that as the tuning voltage is increased, multiple resonance peaks start appearing simply due to the resonance mismatch between the upper and lower rings. To linearize RAMZM, both microrings need to have their resonances matched. This can easily be achieved by 'detuning' one or both of the rings [56]. It is important to note that the spectral response shown in these figures has been de-embedded and normalized for the optical response of grating couplers.

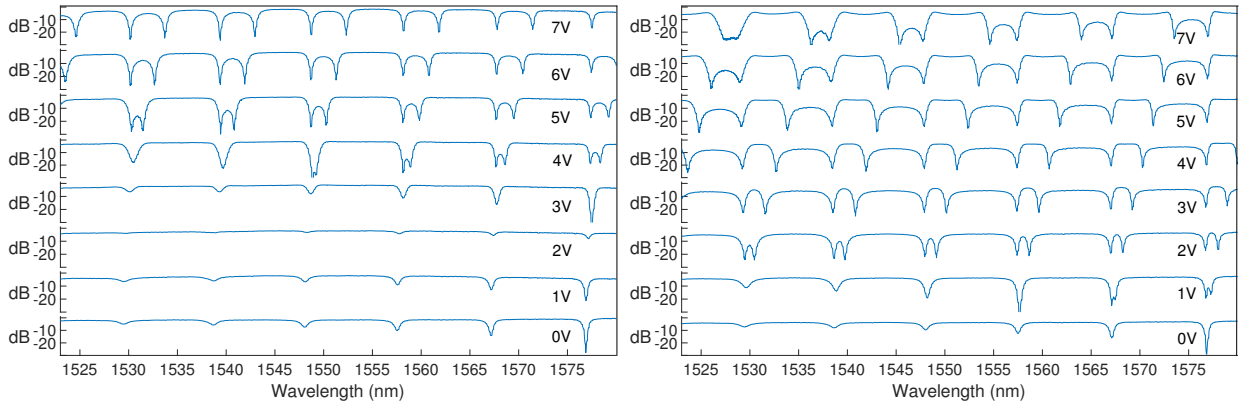

Figure 15: Spectral response of RAMZM (fabricated in IMEC's ISIPP50G SiP process) when (left) lower microring biases and (right) upper microring (θ_{DC}) are tuned by applying 0-7V on a n-doped resistive heater placed around the ring.

The aforementioned bias conditions give us the Taylor series coefficients $\gamma_1 = \frac{1-\tau}{1+\tau}$ and $\gamma_3 = \frac{2\tau^3-7\tau^2+7\tau-2}{3(1+\tau)(\tau^2+2\tau+1)}$. Interestingly, the third-order nonlinearity can be set to zero by enforcing $\gamma_3 = 0$, which is achieved by setting $\tau = \frac{1}{2}$. This ensures that third-order distortion is suppressed, leaving the modulator with fifth or higher odd-order distortions, which are very miniscule in practical application scenarios. The optical power transfer function of a linearized ($\{\phi_{bias}, \theta_{DC}, \tau\} = \{\pi/2, \pi, 0.5\}$)

RAMZM along with the transfer functions of MZMs (both single and push-pull drive [40]) are plotted in Fig. 16. As can be seen, the RAMZM is significantly linear compared to the MZMs when biased in this regime.

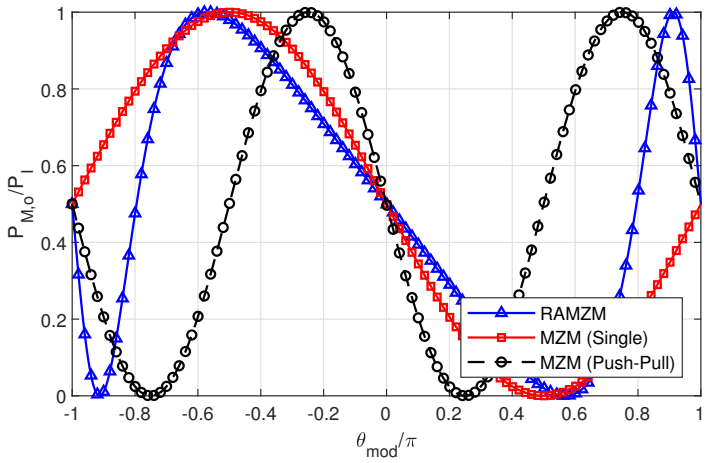

Figure 16: RAMZM, MZM (single drive) and MZM (push-pull drive) Optical Transfer Function as a function of RF voltage induced relative phase shift, θ_{mod}. Here, the RAMZM is biased at $\{\phi_{bias}, \theta_{DC}, \tau\} = \{\frac{\pi}{2}, \pi, \frac{1}{2}\}$ and both MZMs are quadrature biased.

On chip, modulation signal is applied on the high speed p-n phase shifters placed around the microring waveguide as shown in Fig. 13. The input RF signal modulates the carriers present within the microring waveguide, thus modulating the phase of light. This phenomena is known as plasma dispersion effect [4]. When the antiresonance point ($\theta_{DC} = \pi$) is determined at a particular wavelength (1555.55nm in our case), the input signal will modulate the output optical power of RAMZM (as shown in the inset of Fig. 17). In this work, the p-n phase shifters on microrings are biased at 1.125V and differential modulating signal was applied on the rings. The corresponding detected photodiode power exhibits a linear response.

IV-2.3) RAMZM Gain and Slope Efficiency: Now, assuming that a plasma dispersion effect based (depletion or forward-bias mode) phase modulator with linear response is realized (combined effect of plasma dispersion and DC Kerr effect [42]), we express the phase modulation as $\theta_{mod} = \frac{\pi v_m}{V_\pi}$. Here, V_π is defined as the voltage required to achieve π phase shift in the given length of the phase modulator. Now, neglecting higher-order modulation terms, we obtain the RAMZM small signal output optical power as [36]-

$$P_{M,o} = \frac{\pi \gamma_1 P_I v_m}{V_\pi L} \tag{37}$$

Here, the term 'L' is used to include the effects of optical loss. If lossy impedance matching [36] at the input side is implemented, the differential voltage across the modulator is related to the available power by

$$v_m = \frac{v_s}{2} = \sqrt{4 P_{s,a} R_s} \tag{38}$$

Consequently, the small-signal available power gain is given by [36] -

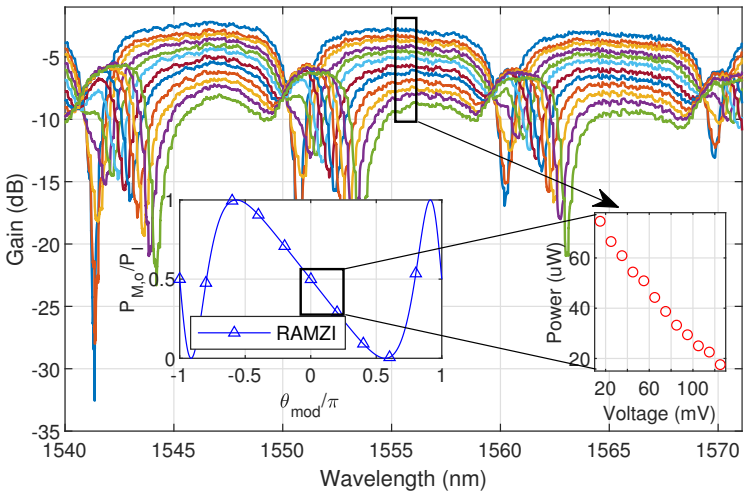

Figure 17: RAMZM spectral response when both upper and lower ring p-n phase shifters are biased at $1.125V$ and applying modulation signal, $\theta_{mod}(v_m)$, on both microring p-n phase shifters in a differential manner. The inset plot on the right shows the modulation of photodiode output power based on $\theta_{mod}(v_m)$ at 1555.55nm. The left inset presents ideal RAMZM transfer function as a function of $\theta_{mod}(v_m)$.

$$G_M = \frac{P_{M,o}^2}{P_{s,a}} = \frac{s_{rmz}^2}{R_s} = \Big[\frac{\pi\gamma_1 P_I R_s}{V_\pi L}\Big]^2 \frac{1}{R_s} \tag{39}$$

where $s_{rmz} \triangleq \frac{P_{M,o}}{v_m} = \frac{\pi\gamma_1 P_I R_s}{V_\pi L} = \frac{\pi P_I R_s}{3V_\pi L}$ (when $\tau = \frac{1}{2}, \gamma_1 = \frac{1}{3}$) is the RAMZM slope efficiency. The effective RAMZM gain can be increased by increasing the input optical power P_I (from a CW laser), reducing the insertion loss L, or decreasing modulator's V_π. To put that in perspective, MZM operating in singe and push-pull drive has the slope efficiencies of $s_{mz} = \frac{\pi P_I R_s}{2V_\pi L}$ and $s_{mz} = \frac{\pi P_I R_s}{V_\pi L}$, respectively.

IV-2.4) Adaptive Calibration of RAMZM: From the earlier discussion, we saw that $\tau = \frac{1}{2}$ i.e. $\kappa = \sqrt{1-\tau^2} = \frac{\sqrt{3}}{2}$ leads to the highest linearity. However, in a practical RAMZM, there will be source of deviations from the ideal condition: (i) optical losses, (ii) process and temperature variations, and (iii) residual nonlinearity from the pn-junction phase modulators. This will lead to a different value of τ for highest linearity (SFDR and IIP3). Thus, an improves RAMZM with tunable ring couplers was designed and taped-out using AIM Photonics process and shown in Fig. 18 with the design parameters in Table 4.

Table 4: Design Parameters of the designed RAMZI modulator in AIM Process

Parameters	**Value**
Racetrack Circumference	2.4mm
% of the Ring loaded with Phase Shifter	60%
Length of the each MZI arm	1.2mm
Coupling Coefficient (κ)	Tunable from 0 to 1
Area	$\sim$0.90mm^2

The tunable coupler is realized using a 2×2 thermo-optic switch which is a library component in the AIM Photonics PDK. The switch can be configured as a coupler by applying voltages to

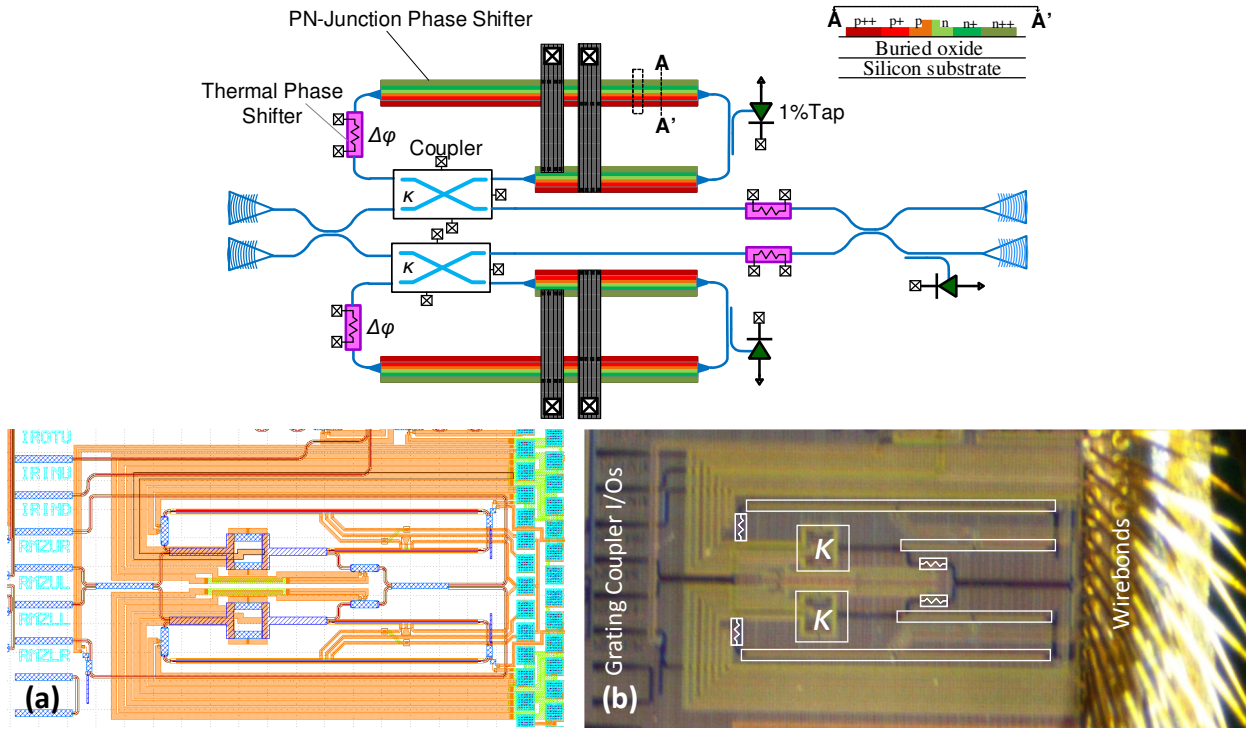

Figure 18: (top) Schematic of the tunable RAMZM modulator. (bottom, a) Layout view of the RAMZM. (bottom, b) chip micrograph of the tunable RAMZM fabricated in AIM Photonics process.

induce phase shifts $[\phi_U, \phi_L] = [2cos^{-1}(\kappa), 0]$ in the upper and lower arms of the thermo-optic MZM. This RAMZM design was intended to be lumped driven (thus the shorter arm lengths of 1.2mm each) to verify the optical domain linearization. The expected EO bandwidth when driven with 50Ω transmission line (or source resistance) is 3-4GHz. The bandwidth can be extended to 10GHz by using a CMOS/BiCMOS low noise amplifier (LNA). Traveling-wave drive will be investigated in future work as it needs careful analysis to avoid undesirable interaction of optical mode with the electrical wavefront.

Fig. 19 shows the experimentally measured drop port response of the rings (left) and bar/cross output of the uncalibrated RAMZM fabricated. Here, it is evident that the actual fabricated device will significantly deviate from the ideal operating point and will require rigorous adaptive calibration. To facilitate automatic adaptive calibration scheme, optical taps (1% or 10%) are placed on each ring and RAMZM output (cross) port followed by monitor photodetector (PD) as seen in Fig. 18(top). The photodetector's current output is fed to a transimpedance amplifier (TIA) followed by a 16-bit ADC. Our tuning algorithm takes the ADC output digital code as input argument and set the tunable coupler, ring and quadrature biases at their desired operating point by tuning the on-chip thermal phase shifters by means of a 16-bit ***Digital-to-Analog Converter (DAC)*** in a closed loop. This instrumentation is discussed later in Section III-5.

First, the tunable couplers on both rings are set for zero coupling (Fig. 20b) by observing the monitor PDs placed on each ring. This effectively decouples the rings from the MZM arms. Utilizing this as a reference point and referring back to the characterization data of standalone tunable coupler, the appropriate coupling coefficient is set. Fig. 20c shows the spectral response of the RAMZM when the upper coupler is biased for target coupling coefficient whereas Fig. 20d shows the response after both coupler is set. Afterwards, RAMZM is biased at antiresonance point

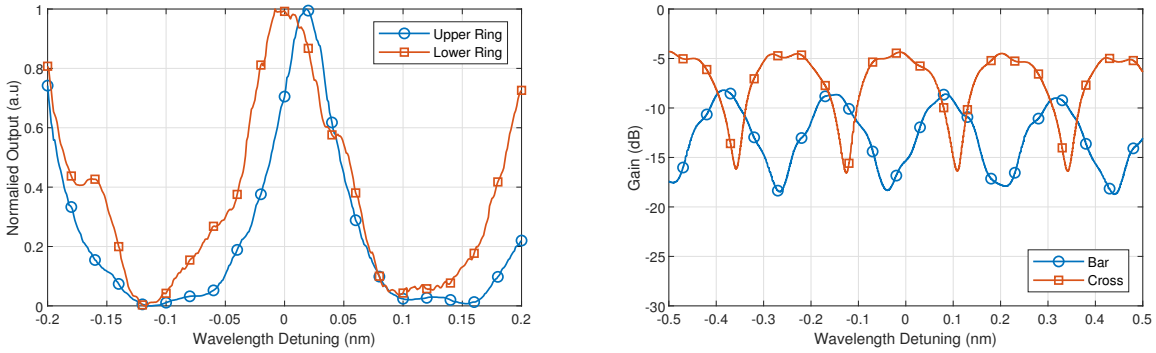

Figure 19: Normalized misaligned drop port response of upper and lower ring (left), misaligned bar/cross port response (right) of the RAMZM fabricated in AIM Photonic's SiP process.

by means of searching minimum drop port response of the rings at the target frequency of operation (Fig. 20e). Finally, the quadrature bias is set by means of heater placed on the RAMZM arm and monitor PD placed at the cross port of RAMZM. Due to thermal crosstalk, setting DAC voltages at each step requires all previous steps to be repeated since the newly set heater alters previously set bias points. The entire calibration algorithm is recursive in nature and is run multiple times until all the bias points converges within a certain tolerance level.

To demonstrate linearized modulation capability of the calibrated RAMZM, static modulation response has been recorded and shown in Fig. 21. Here, differential bias voltages ($v_{diff} = v_{RF(UR)} - v_{RF(LR)}$) have been applied to RAMZM and corresponding spectral response have been presented. It is evident from the plot that the modulation response is highly linear.

IV-2.5) Second and Third-order Intercept Point From Eq. 31, the optical power of the third-order intermodulation distortion for a two-tone input, $\theta_{mod} = \frac{\pi V_m}{V_\pi} \cdot [sin(\omega_1 t) + sin(\omega_2 t)]$, can be written as $P_{optical-im3} = \frac{P_I}{L} \cdot \frac{3\gamma_3}{4} \cdot (\frac{\pi V_m}{V_\pi})^3 cos(2\omega_1 \pm \omega_2)$ at $2\omega_1 \pm \omega_2$ [36]. On the other hand, its fundamental counterpart can be expressed as $P_{optical-fund} = \frac{P_I}{L} \cdot \gamma_1 \cdot (\frac{\pi V_m}{V_\pi}) cos(\omega_1)$ at ω_1. We derive the third-order input-referred intercept point, IIP_3, for the RAMZM as

$$IIP_3 = \frac{2V_\pi^2 \left[\tau^2 - 2\cos(\theta_{DC})\tau + 1\right]^2}{\pi^2 R_s \left[2\cos(\theta_{DC})^2\tau^2 + (\tau^3 + \tau)\cos(\theta_{DC}) + 2\tau^4 - 8\tau^2 + 2\right]} \tag{40}$$

We also derived the second-order intercept as

$$IIP_2 = \frac{V_\pi^2 \left[\tau^2 - 2\cos(\theta_{DC})\tau + 1\right]^2}{2\pi^2 R_s (\tau^2 - 1)^2} \cdot \tan(\phi_{bias})^2 \tag{41}$$

From these expressions, it can be noted that both IIP_2 and IIP_3 are strong functions of V_π. Also, the IIP_3 of an RAMZM is independent of the arm bias (ϕ_{bias}), but strongly dependent upon ring bias (θ_{DC}) and the coupling ratio. On the other hand, unlike IIP_3, IIP_2 strongly depends upon arm biasing. To show the dynamic characteristics, relative power of the fundamental, IM_2 and IM_3 are plotted against the modulation angle of the RAMZM in Fig. 22(left). Here, 1st, 2nd and 3rd derivatives of the RAMZM transfer function are calculated to find the relative power of the fundamental, IM_2 and IM_3 distortions considering $\{\phi_{bias}, \theta_{DC}, \tau\} = \{\frac{\pi}{2}, \pi, \frac{1}{2}\}$. Here, we see that for small modulation stimulus, the IM_2 and IM_3 are virtually non-existent.

As discussed before, MZM suffers from higher nonlinearity due to its sinusoidal transfer function. To quantify the linearity of both MZM and linearized RAMZM, $SFDR_3$ is calculated in Fig.

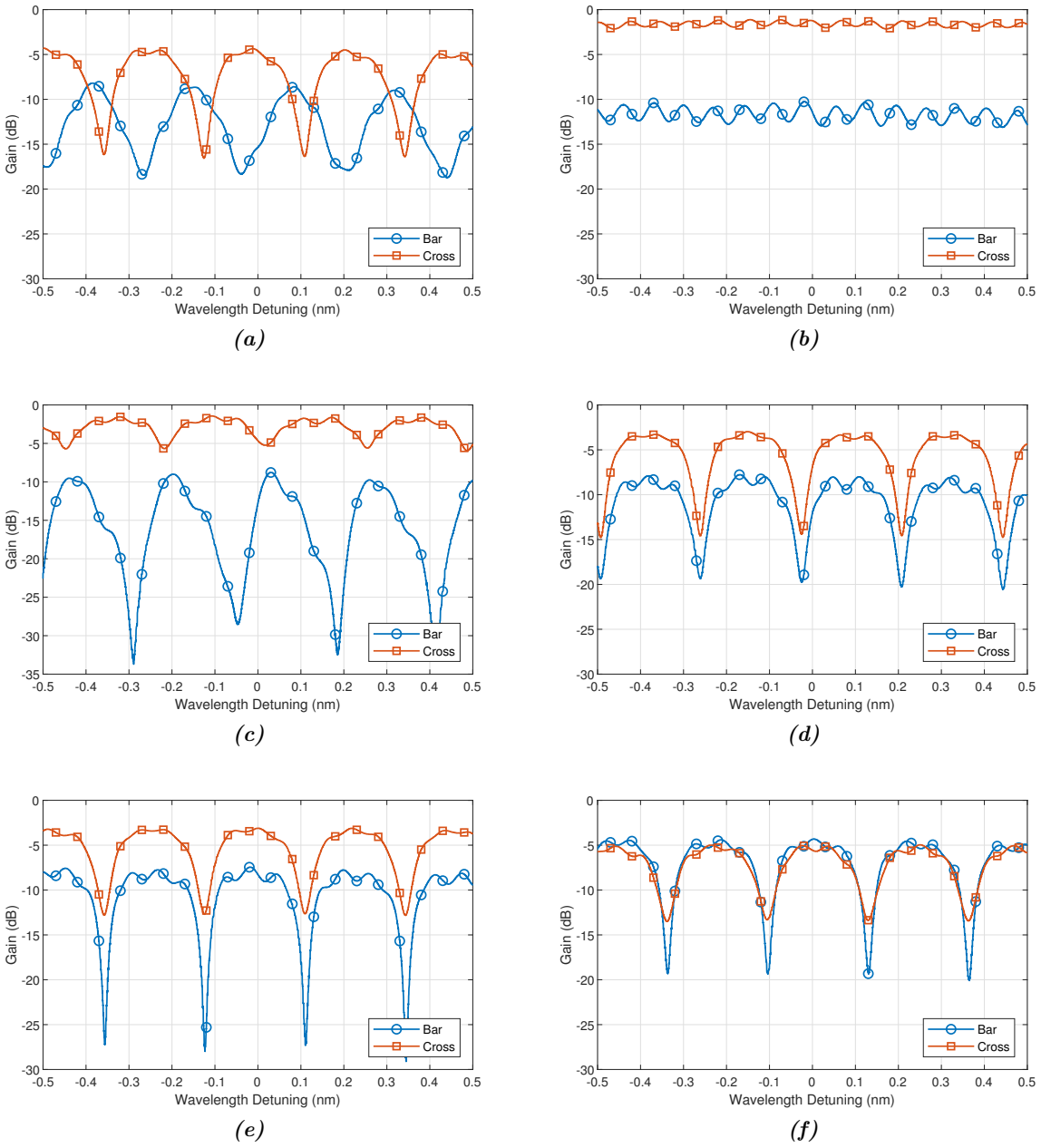

Figure 20: Spectral response of RAMZM bar and cross port (a) before calibration (b) after upper and lower ring is decoupled from the RAMZM arms (c) after upper tunable coupler is tuned (d) after lower tunable coupler is tuned (e) after both ring resonances are aligned (f) after quadrature bias tuning. Here, the grating coupler response has been de-embedded from the actual recorded data.

22(right). Here, RAMZM and MZM have SFDR values of 128.16 and 109.94 $dB/Hz^{\frac{2}{3}}$ at 1GHz, respectively. This is 18dB improvement over regular MZMs, which makes RAMZM very attractive for high-performance RF photonic applications. Note that these are simulation results based on compact modeling of RAMZM. Two-tone experimental characterization will be performed soon using our new 50GHz Vector Network Analog (VNA) with dual source and two-tone IMD capability. The results will be reported in future publications and the sponsor (AFOSR) will be acknowledged.

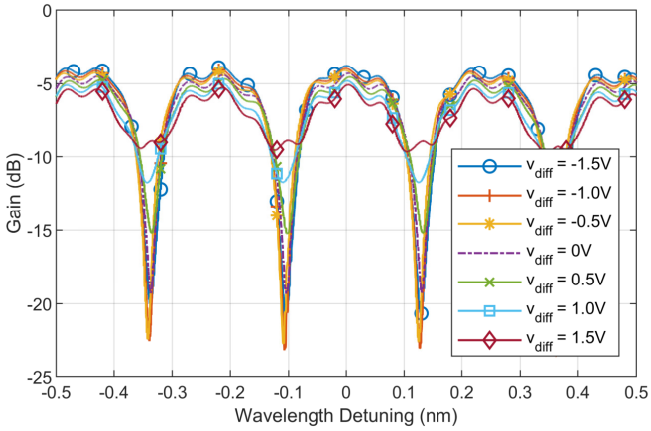

Figure 21: Static response of RAMZM for various differential voltages.

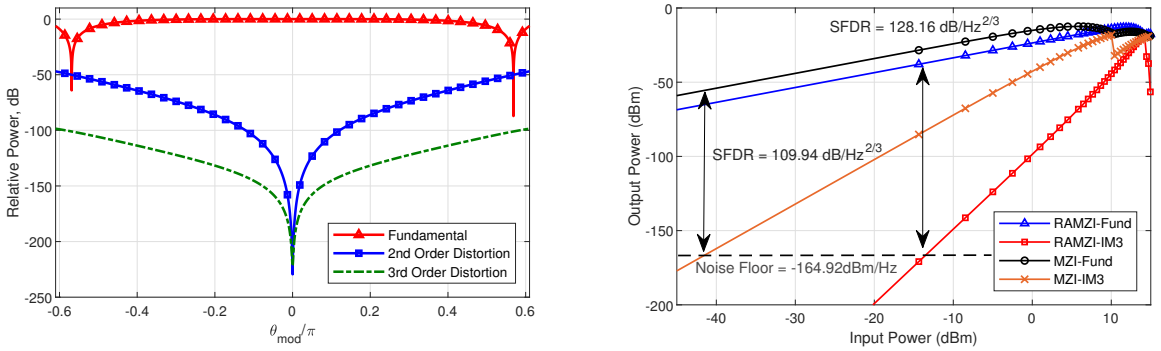

Figure 22: (left) RAMZM Fundamental, second and third-order distortion components *vs* ring modulation angle, θ_{mod}. Here, the RAMZM is biased at $\{\phi_{bias}, \theta_{DC}, \tau\} = \{\frac{\pi}{2}, \pi, \frac{1}{2}\}$. (right) SFDR performance of RAMZM and MZM in a Photonic Link. Here, RAMZM and MZM bias conditions are $\{\phi_{bias}, \theta_{DC}, \tau\} = \{\frac{\pi}{2}, \pi, \frac{1}{2}\}$ and $\{\phi_{bias}\} = \{\frac{\pi}{2}\}$, respectively.

V. Research Objective 3: Tunable RF Photonic Filters

V-1. Tunable Optical Filters

A tunable bandpass filter over a wide range of spectrum is essential for realizing software defined radio (SDR). Silicon photonics has enabled the potential for chip-scale photonic filters with high selectivity and extremely-wide tuning range over the whole free spectral range (FSR), spanning 10s of GHz. This can lead to compact wideband RF photonic front-ends. Here, CMOS electronics will be leveraged for rapid filter reconfiguration and calibration to mitigate the process voltage and temperature (PVT)-dependent variations. In this work, a hybrid optical filter was designed around 1550 nm wavelength using AIM Process Design Kit (PDK) and our custom developed modeling framework. Since the RF photonic filter is designed using passive components in the signal path, it is perfectly linear with the overall linearity set by the RF-to-optical modulator. Furthermore, the filter size is significantly reduced compared to discrete photonics and can be fitted on chip-scale form factors.

Fig. 23 (left) shows a fourth-order filter using all-pass filter (APF) synthesis with symmetric top and bottom ring-loaded arms [30, 32]. Earlier, we presented rapid simulation of these filters

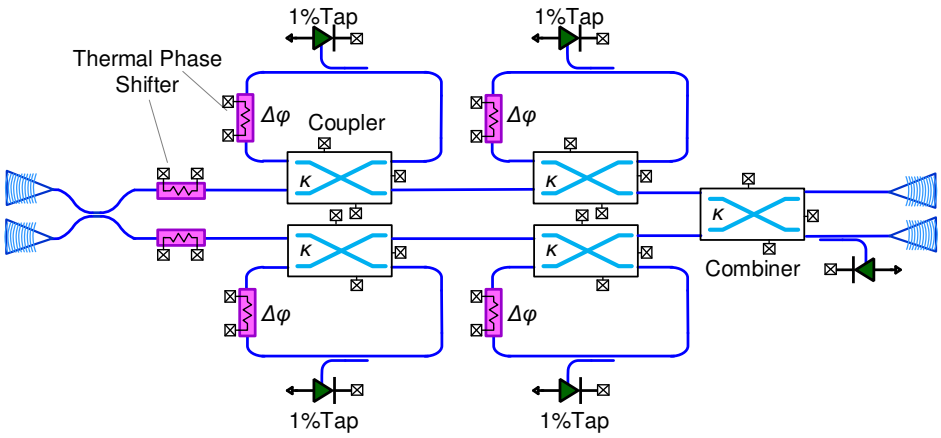

Figure 23: Schematic of the a fourth-order APF-type optical filter with tunable parameters.

in ***Section*** III-2 of this report. Each arm has two low-loss cascaded racetrack resonators (with circumference around 2mm for 28GHz FSR) and phase shifters, with two couplers resulting in individual APFs. The couplers and the output combiner are realized using the 2×2 thermo-optic switch in the AIM PDK. The output combiner simultaneously evaluates the sum and difference of the phase shifts produced by the two APFs, which can implement any filter polynomial, i.e. Butterworth, Inverse Chebyshev, Elliptic, etc. 1% optical feedback taps are placed at critical positions, i.e. rings and one of the outputs, for the tuning algorithm. The simulated spectral response of the filter is shown in ***Fig.*** 25 (right). As can be seen from the spectral response, this filter has stopband rejection of more than 35dB. Furthermore, the whole filter response can be translated across the whole frequency range by tuning the phase shifters in synchrony, with an adaptive algorithm to maintain the filter shape.

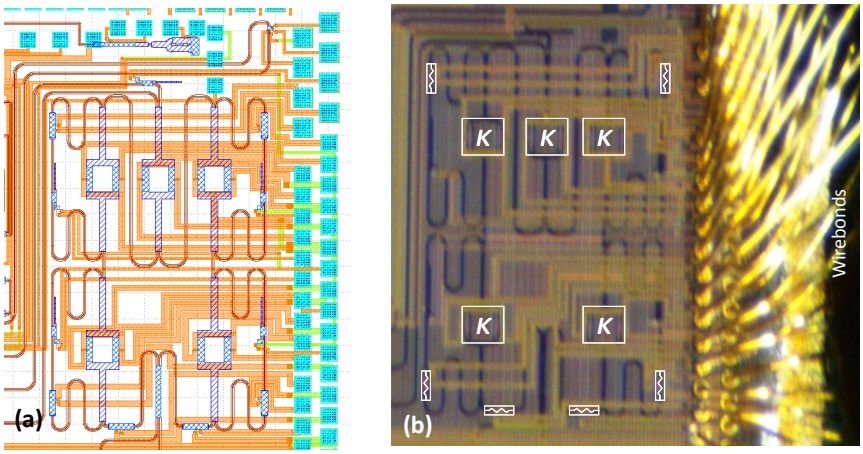

Figure 24: (a) Layout view of the RAMZM, (b) chip micrograph of the tunable RAMZM fabricated in AIM Photonics process.

V-2. Filter Reconfiguration Algorithms and Challenges

As mentioned above, the silicon photonic devices are sensitive to PVT variations. Furthermore, in order to realize flexible wideband receivers, the filter needs to be reconfigurable, meaning that the filter is capable of operating at different frequencies with any arbitrary bandwidth and stop-

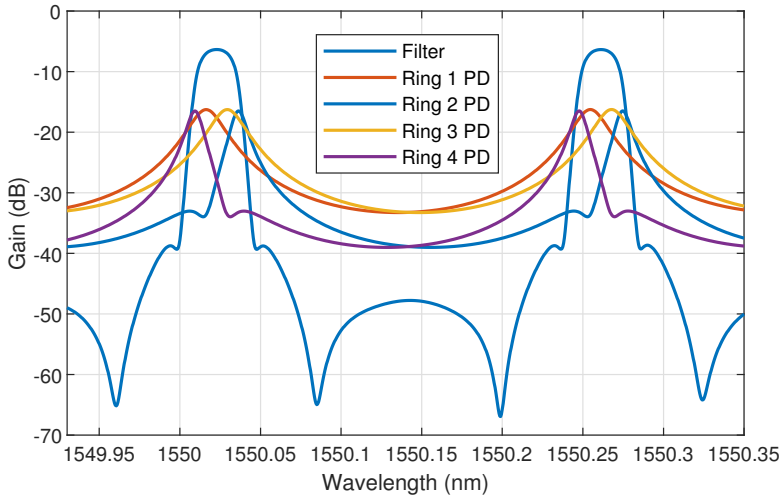

Figure 25: Simulated frequency response of the fourth-order APF-type filter seen in Figs. 23 and 24. Optical monitors are realized using the 1% taps and are used for setting the desired resonant frequency of the individual rings, values of the couplers, and phase shifter settings in the optical filter. The filter can be tuned to realize any fourth-order filter characteristic polynomial response with any center frequency.

band rejection specified by the user. This requires tuning of several photonic components such as thermal phase shifters and couplers. Therefore, in this current filter, electronic feedback was be employed, using optical ports terminated into on-chip photodetectors, to adaptively tune the phase shifters in the forward path. For reconfiguration, the APF synthesis algorithm is used to determine the coupling ratios (κ's) and phase shift values ($\Delta\phi$'s) [30,32]. Each phase shifter in the four rings and two input arms is controlled using 16-bit current DACs that can supply upto 17mA current. The DAC current range is sufficient to achieve a full π phase shift in the thermal phase shifters. As discussed later, the digital tuning of filter is controlled by an algorithm that runs on an Arduino/Matlab interface. The algorithm can also be ported to an FPGA or an ASIC in case the design is converted into a product.

The filter reconfiguration algorithm proceeds as follows: To set the initial filter response, a tunable laser is used to generate input tones at the desired frequency(wavelength) locations, governed by a look-up table generated using the synthesis algorithm [2, 30, 32]. The detector taps sense the optical filter response which are converter to a voltage by a transimpedance amplifier (TIA). A 16-bit ***analog-to-digital converter (ADC)*** is used to digitize the monitor outputs. These values are used by the filter tuning algorithm in the digital backend to tune the rings and phase shifter responses at the desired frequency (wavelength) locations. This initial configuration is stored and then used for rapid filter center frequency tuning across the desired bands.

We are currently in the process of fine-tuning the filter-tuning algorithms and their testing on the fabricated packaged PIC. Two major challenges in filter tuning are:

- ***Thermal crosstalk:*** Thermal crosstalk between the phase shifters leads to the response of the filter components to shift as the algorithm progresses. This requires all the phase shifters to be updated at each tuning step, instead of tuning each of the rings individually. We employed thinning of dices to 150μm, which is the minimum allowed by our packaging vendor, and used a ***thermo-electric cooler (TEC)*** to maintain a stable background temperature, which helps reduce the crosstalk between elements [32]. A least-mean square (LMS) algorithms is being fine-tuned to stabilize filter tuning.

- ***Coupling coefficient tuning:*** A major challenge is accurately setting the coupling cofficients (κ's) for each of the rings. While we can set the resonant wavelength easily by monitoring the monitor port response, setting a desired κ to match the value from the synthesis algorithms, the presence of ***process and temperature (PT)*** variations, is non-trivial. Previous works used the critical coupling point of the ring as a reference and then backtracked using the pre-characterized *kappa vs* $V_{\Delta\phi}$. Here, $V_{\Delta\phi}$ is the voltage applied to the thermal phase shifter [32]. Such methods employed an ***optical vector network analyzer (OVNA)***, different than the electrical VNA. Our methods are circumventing the need for an OVNA for full integration with on-board electronics.

Fig. 26 shows the current experimental results in filter tuning. We can see that the filter response is taking shape and >40dB notches are feasible. As mentioned earlier, we are currently working on fine-tuning the algorithm against the thermal crosstalk and *kappa* tuning with PT variations. The results will be reported in future publications and the sponsor (AFOSR) will be acknowledged. In future efforts, the algorithm will be changed to use a tunable RF frequency synthesizer, instead of the tunable laser, for full integration on a chip.

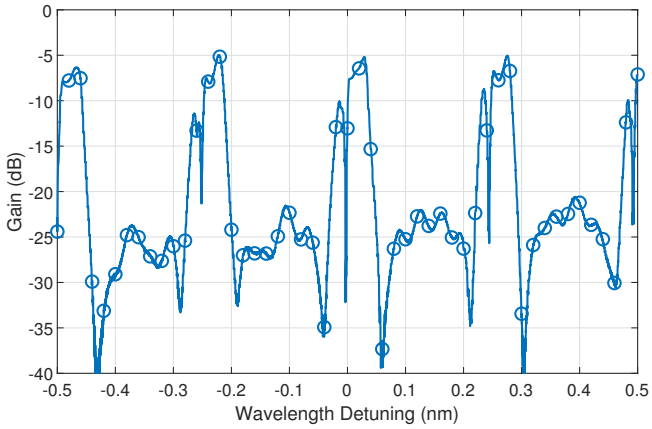

Figure 26: Experimentally measured fourth-order APF-type filter response. The algorithms are being fine-tuned to compensate for thermal crosstalk on the chip which will improve out-of-band suppression.

V-3. Reconfigurable RF Photonic Filters based on Programmable Mesh

We further extended the tunable RF filter design to a fully programmable mesh architecture. A 4×4 mesh as shown in ***Fig.*** 27 was designed in the PIC taped-out using the AIM Photonics process. The mesh is constructed using 2×2 thermo-optic switches seen earlier which can be configured in the cross and bar states, phase shifters, and tunable couplers depending upon the electrical DACs outputs [57]. The mesh is comprised of rectangular cells of size $a\times b\approx 600\mu m\times 760\mu m$. The thermo-optic switches have a sub-20μs switching time-constant, low insertion loss (<0.25dB), and low tuning power ($\frac{35mW}{\pi}$ phase-shift) [3]. The smallest ring circumference is $L=2(a+b)=2.72mm$ which sets the free-spectral range, $FSR=\frac{c}{n_gL}\approx 26GHz$.

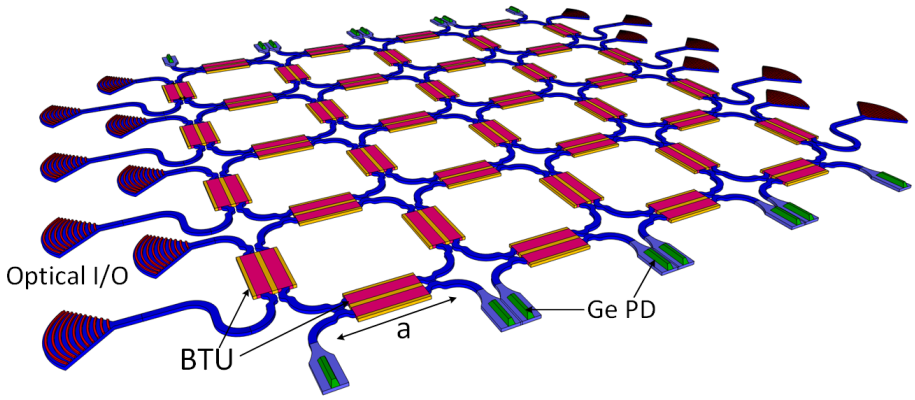

Figure 27: 3D visualization of a passive 4×4 programmable mesh. Here, the electrical wires for the thermal tuners are not shown. The Ge detectors are placed at the North-South and optical I/Os are on the East-West.

The switch cell seen in Fig. 27 has its output and input electric fields related by the equation [57,58]:

$$\begin{bmatrix}E_{o1}\\E_{o2}\end{bmatrix}=Ce^{j2\pi f\Delta\tau}\begin{bmatrix}E_{i1}\\E_{i2}\end{bmatrix} \tag{42}$$

with the coupling matrix expressed as

$$C=-je^{j\phi_A}\begin{bmatrix}sin(\phi_D) & cos(\phi_D)\\ cos(\phi_D) & -sin(\phi_D)\end{bmatrix} \tag{43}$$

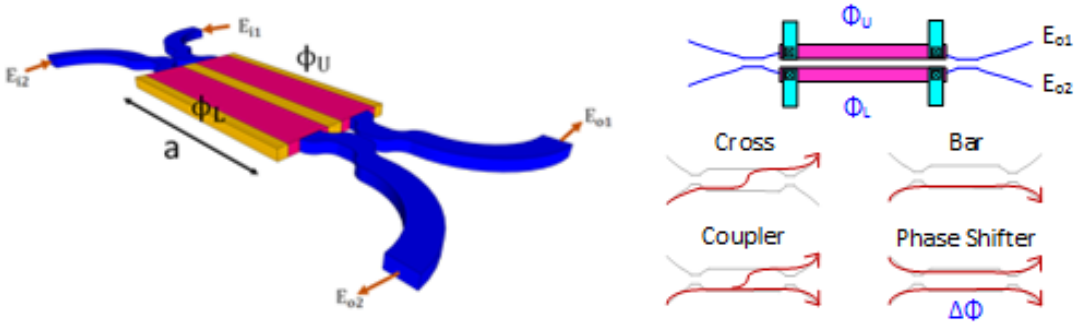

Figure 28: 3D visualization of the 2×2 thermo-optic switch tiled to build the optical mesh.

Here, $\phi_A = \frac{\phi_U + \phi_L}{2}$ and $\phi_D = \frac{\phi_U - \phi_L}{2}$ are the phase terms that depend upon the phase shifts, ϕ_U and ϕ_L, in the upper and lower phase shifter respectively. The additional phase term in Eq. 42, $e^{j2\pi f \Delta\tau}$ is due to the frequency-dependent propagation delay in the switch due to its long length. The switch can be configured into one of the several elements by appropriately selecting the phase shifts ϕ_U and ϕ_L. Table 5 shows the required values of $[\phi_U, \phi_L]$ to configure it as a: (i) tunable coupler with field cross-coupling coefficient (κ), (ii) switch in the bar state, (iii) switch in the cross-state, and (iv) a two types of phase-shifters. The Type-I phase-shifter provides a phase-shift (of θ radians) in the bar state and the Type-II phase-shifter provides a phase-shift in the cross state. Both these phase-shifters are uniquely utilized in specific application circuits.

Table 5: Thermo-optic switch configuration as coupler, switch, Type-I or II phase shifters.

Element	Parameter	$[\phi_U, \phi_L]$	Coupling Matrix, C
Tunable Coupler	$\kappa = cos(\phi_D)$	$[2cos^{-1}(\kappa), 0]$	$-je^{j \cdot cos^{-1}(\kappa)} \begin{bmatrix} t & \kappa \\ \kappa & -t \end{bmatrix}$
Bar State	$\kappa = 0$, $\phi_D = \frac{\pi}{2}$	$[\pi, 0]$	$\begin{bmatrix} 1 & 0 \\ 0 & -1 \end{bmatrix}$
Cross State	$\kappa = 1$, $\phi_D = 0$	$[0, 0]$	$-j \begin{bmatrix} 0 & 1 \\ 1 & 0 \end{bmatrix}$
Phase Shifter, Type-I (Bar)	$\phi_A = 0$ and $\phi_D = \frac{\pi}{2}$	$[\frac{\pi}{2} + 0, 0 - \frac{\pi}{2}]$	$-j \begin{bmatrix} e^{j\theta} & 0 \\ 0 & -e^{j\theta} \end{bmatrix}$
Phase Shifter, Type-II (Cross)	$\phi_A = 0$ and $\phi_D = 0$	$[0, 0]$	$-j \begin{bmatrix} 0 & e^{j\theta} \\ e^{j\theta} & 0 \end{bmatrix}$

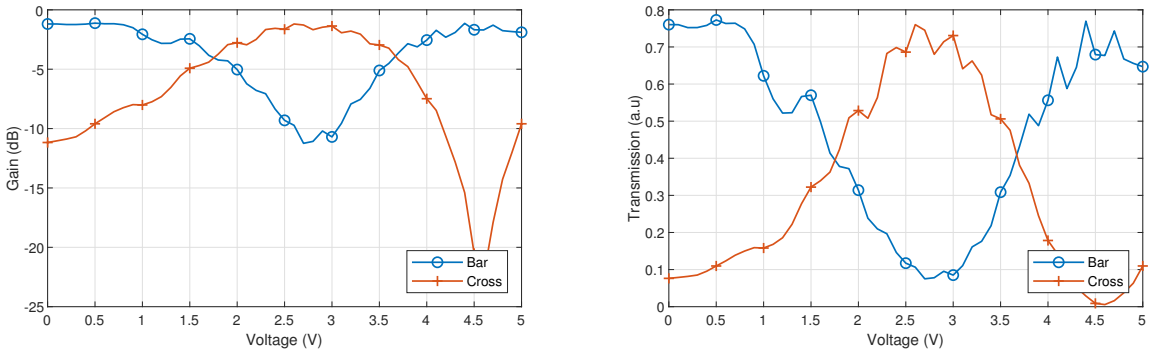

Figure 29: (left) Experimentally measured phase shift versus applied voltage for an arbitrary thermo-optic phase shifter, (right) Transmission characteristics of the 2×2 switch as a function of the applied voltage.

The thermal phase shifters allow tuning of passive optical elements with a small footprint. Doped waveguide resistors are employed for Joule heating of the waveguide sections. Since the effective index is dependent upon temperature, which in turn depends upon the voltage (or current) applied across the heater, an optical phase shift is produced [3]. Due to Joule heating dependent mechanism, the optical phase shift is a non-linear function of the applied voltage, $\Delta\phi(V)$ as shown in **Fig.** 29 (left). As a result, the 2×2 thermo-optic switchincurs a non-linear relationship between applied voltage and phase shifter ϕ_U and ϕ_L. The transmission characteristics of the switch is shown in **Fig.** 29 (right). This non-linear relationship between voltage pair $[V_U, V_L]$ and the corresponding phase-shifts $[\phi_U, \phi_L]$ may vary from across process corners and must be taken into account during

the automatic reconfiguration of optical circuits on SiROAP. For the Type-II phase-shifter, the upper and lower phase shifter inputs in the switch can be tied together to create the phase shift of θ, the collapsing the two degrees of freedom into one. This is easier to control on the chip, especially with nonlinear relationship between the applied voltage and the phase-shift in thermal phase shifters [59].

Due to PVT variations in the switches, optical monitors (which are essentially slower photodetectors) are necessary for automatic configuration and tuning of the optical circuits that are realized on the 2D mesh. In a most cautious design, a 1% optical monitor tap can be placed at every corner in the mesh, at the cost of higher mesh loss, and more electrical pads. In **Fig.** 27, Ge detectors were placed at the North-South edge of the mesh to provide sensed signal to the feedback loop that would be used to configure the DACs that control the switches. **Fig.** 30 shows the simulated results from a mesh realized using AIM PDK cells and Lumerical Interconnect software. The 2D mesh can be configured to implement a large variety of RF photonic filters: Ring resonators, CROW filters, All-pass decomposition-based filters, and FIR filters, etc.

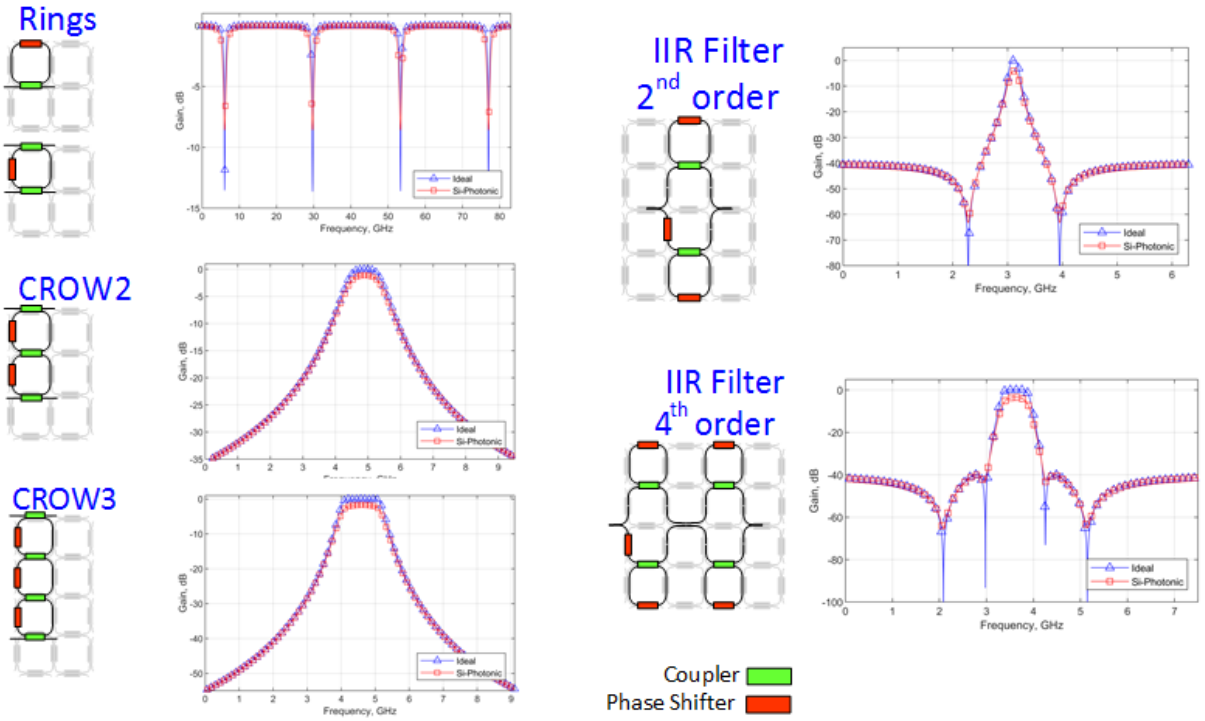

Figure 30: Several optical filter topologies realized using the 4×4 mesh. The simulations are performed using actual AIM PDK cells using Lumerical's Interconnect system-level simulation software.

The 4×4 mesh was taped-out and fabricated using AIM Photonic's MPW and the layout and chip micrographs are shown in Figures 31 and 32 respectively. The chip is being packaged on a different custom designed PCB and a larger interfacing board for hardware prototyping is being designs. Experimental results from the mesh should be available in a few months. The results will be reported in future publications and the sponsor (AFOSR) will be acknowledged.

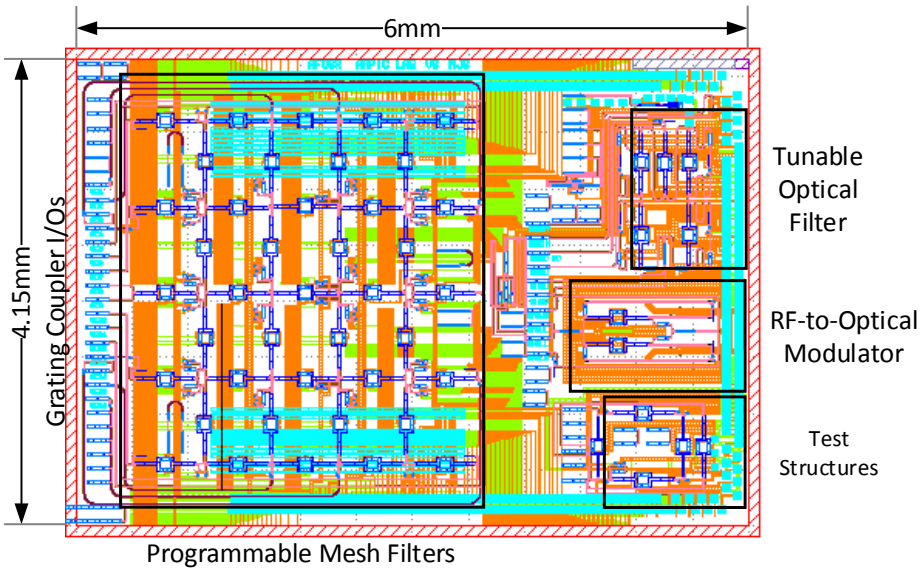

Figure 31: Full chip layout of the chip fabricated using AIM photonic process.

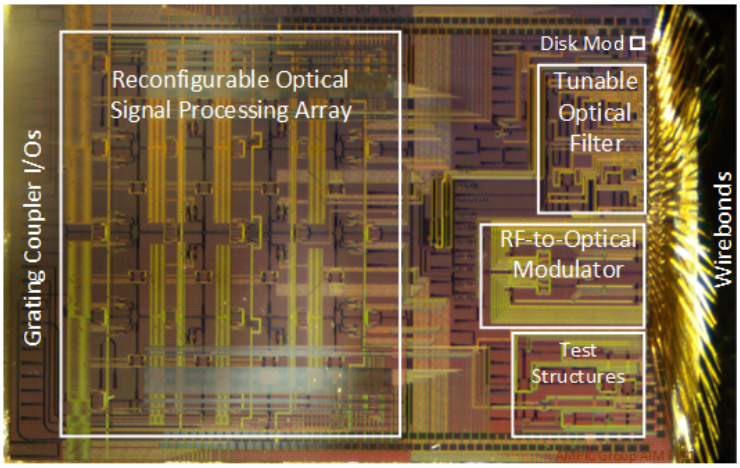

Figure 32: Full chip micrograph of the chip fabricated using AIM photonic process.

VI. Research Objective 4: System Prototyping and RF Photonic Link Analysis

VI-1. Chip Packaging and Hardware Prototyping:

We developed generalized hardware that allows testing of complex photonic integrated circuits (PICs). The architecture of the PC board is shown in ***Fig.*** 33. The board is able to provide several channels (M in number) programmable voltage/currents (up to 5V or supplying up to 17mA to 250 Ω resistive load offered by the thermal tuner) and sense a large number (say N) analog channels. The voltage/current channels are realized using parallel DAC chips and the sensing is performed using multi-channel ADC chips. We are able to set the DAC channels and read ADC channels using a low latency Arduino software code, which is called as functions from high-level algorithms, implemented in Matlab or Python, that tune the PIC device under test (DUTs).

The PIC will is packaged on a daughter board using ***chip-on-board (COB)*** packaging, shown in ***Fig.*** 34, which connects to the main PC board using high-density ribbon connectors. The board

uses a 32-bit Arduino Due controller that in-turn uses the SPI bus interface with the DACs and ADCs to set and read voltages. We developed functions in Arduino code to write digital code into the DACs to produce the required voltages and read the sensed ADC voltages in the form of digital codes. The high-level algorithms are implemented in Matlab on a PC which communicates with the Arduino controller on a USB interface.

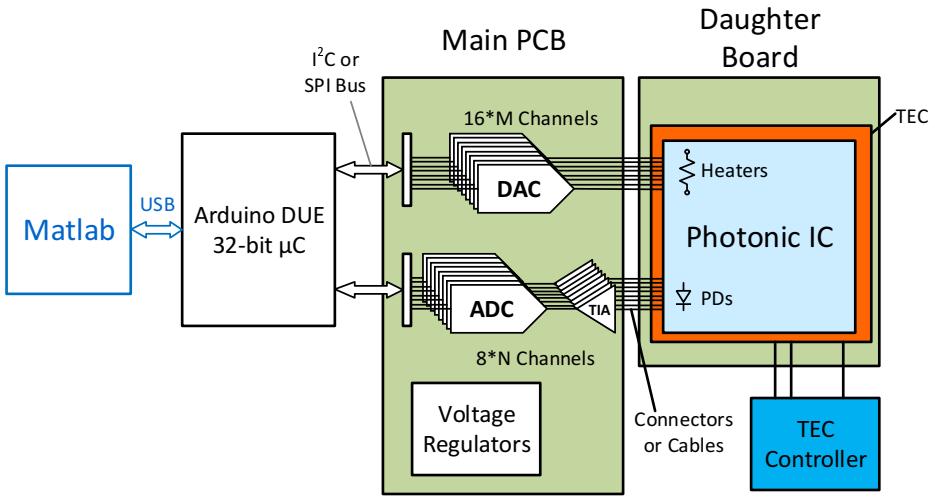

Figure 33: PIC Test Instrumentation Architecture using for experimental characterization.

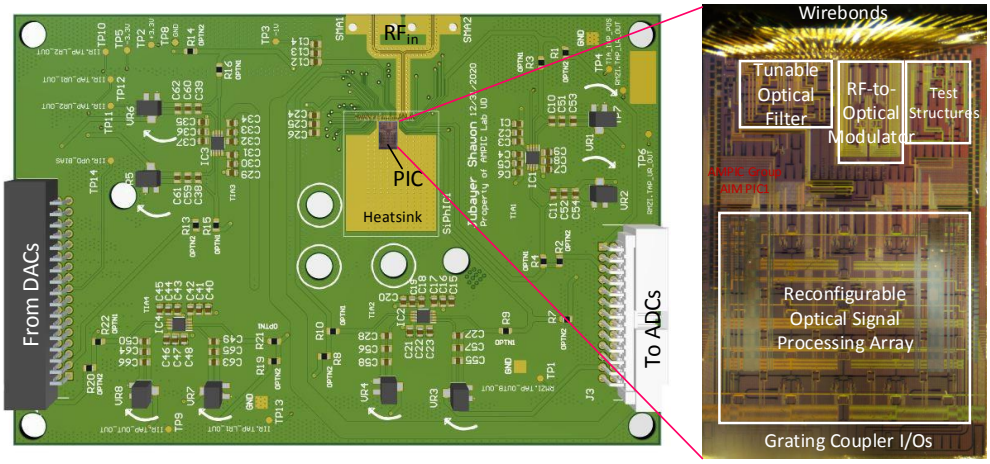

Figure 34: Chip-on-board packaged PIC on the daughter board PCB. The 25mm^2 chip was fabricated in the AIM Active Photonics process and then packaged using a commercial vendor. Light is coupled in and out of chip using Fiber Arrays using an optical alignment setup.

Fig. 35 shows the experimental setup for characterizing the packaged PICs. This features a custom assembled optoelectronic probe station for simultaneous optical and RF probing. This setup includes an automatic optical alignment and probe station on an optical table. The optical alignment setup is controlled by a MATLAB-driven software platform. The automatic alignment facilitates rapid and repeatable testing of photonic components using automation scripts. Optical measurement capabilities include Agilent 8164 Lightwave mainframe with a Keysight compact tunable laser and high-speed detectors. Two microscope cameras are employed for the top and lateral views with their associated imaging software.

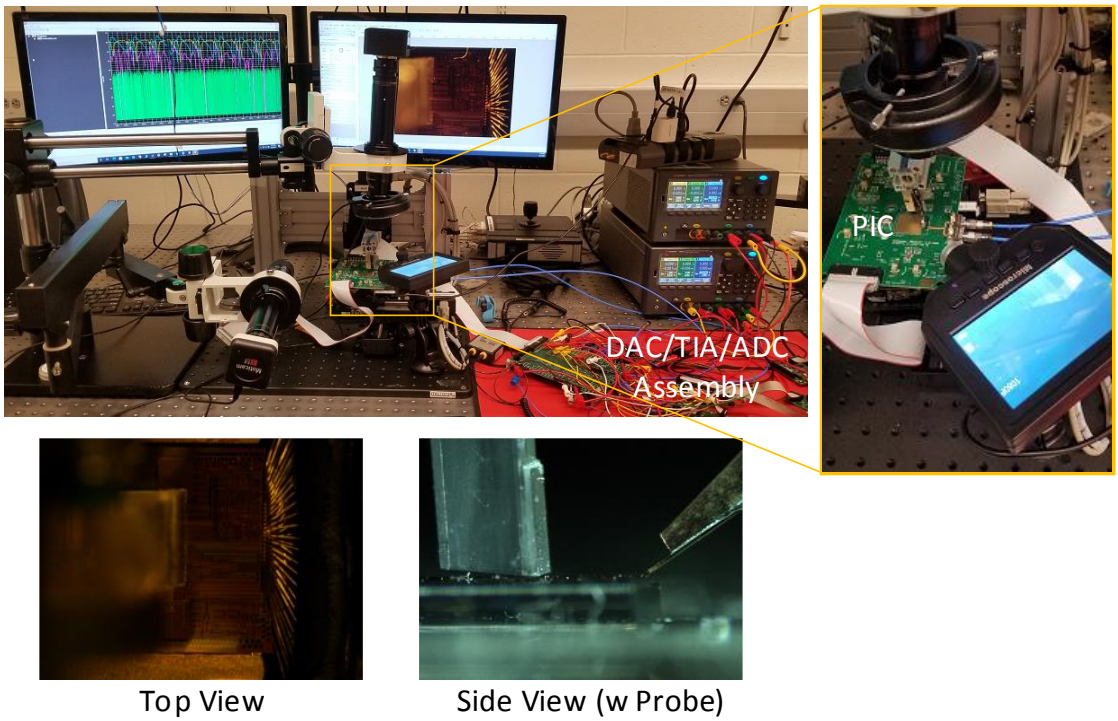

Figure 35: Experimental setup with optical alignment of fiber arrays to the on-chip grating couplers. The custom built setup rests on a floated optical table and uses automatic controlled X-Y stages, a manually tuned R-θ fiber array holder, and top and side view microscopes. The setup also admits DC and RF probing of dices.

Fig. 35 shows the fabricated AIM chip with vertical and side microscopic camera views. 8-channel fiber arrays are used for alignment with vertical couplers on-chip while electrical signals are applied either using RF probe or wire-bonds in the case of packed PICs. RF Photonic measurements are performed using 50GHz Keysight PNA-series VNA with two-tone intermodulation measurement capability and low phase noise synthesizer. A 50GHz bandwdith photodetector from Discovery Photonics is used for the optical to electrical conversion. Modulator transient measurements are performed using Keysight 4903B 12.5 Gbps BERT and waveform generator and Keysight 86100D Wide-Bandwidth Oscilloscope with 86103D 50 GHz optical / 30 GHz electrical module. Filter measurements are peformed using wavelength sweeps using the tunable laser and detectors. Electrical I-V characteristics of devices such as thermal phase shifters are obtained using SMUs.

VI-2. RF Photonic Link Analysis and Tradeoffs

An analog RF photonic link based on linearized RAMZM presents a multi-corner tradeoff between gain, noise figure, linearity and power consumption. This was analyzed in this project, and a journal manuscript is under review [60] which is summarized in this section. An analog optical link using RAMZM is shown in Fig. 36 (a). Here, P_I and $P_{M,o}$ are the optical power at the modulator input and output respectively. $P_{s,a}$ is the input RF power, $P_{o,d}$ and P_L are the optical and then detected RF power at the receiver. Fig. 36 (b) shows the small-signal noise model for the analog optical link seen in Fig. 36. The link parameters used for the subsequent numerical analysis are provided in Table 6. These link parameters are on par with the Silicon Photonic components that are available from foundry PDKs [61, 62].

As seen in Fig. 36, the two rings in the modulator present differential lumped capacitive load, C_M, with series electrode resistance, r_M. Thermal noise is contributed by the input source resistance (R_s) with noise power $kT\Delta f$. The series electrode resistances, r_M, also contributes thermal noise.

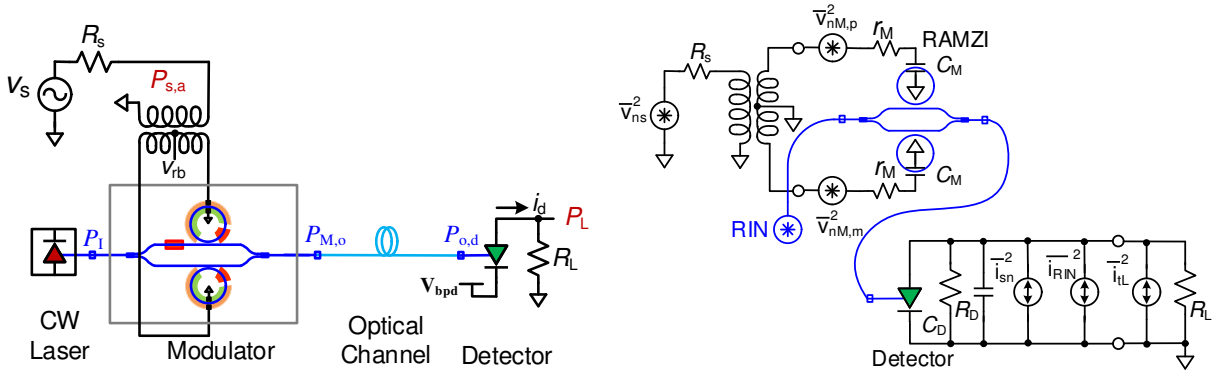

Figure 36: (a) An analog optical link using RAMZI modulator (RAMZM). (b) Small-signal noise model for the analog optical link employing the RAMZM.

Table 6: Analog Optical Link Parameters

Parameter	Value	Unit
Laser input power (P_I)	13	dBm
Laser Relative intensity noise (RIN)	-145	dB/Hz
Modulator V_π	5	V
Modulator Insertion loss (IL)	10	dB
Source Impedance (R_s)	50	Ohm
Detector responsivity (r_d)	1.1	A/W
Load Impedance (R_L)	50	Ohm
BW	1	Hz

The resulting mean square noise voltage across each C_M is simply $\frac{kT}{C_M}$. The net input-referred mean square noise voltage is

$$\overline{v_{n,in}^2} = \overline{v_{nM,p}^2} + \overline{v_{nM,m}^2} = \frac{kT}{C_M} + \frac{kT}{C_M} = \frac{2kT}{C_M} \tag{44}$$

The corresponding noise power at the RAMZM output would be $s_{rmz}^2 \frac{2kT}{R_s C_d}$. This can be interpreted as if net thermal noise is equal to the input noise power $kT\Delta f$, with the corresponding bandwidth $\Delta f = \frac{1}{2\pi(R_s+2r_M)\cdot C_M/2} = \frac{1}{\pi(R_s+2r_M)\cdot C_M}$.

VI-2.1) Optical Channel and Detector: Once the RF signal is converted into the optical domain, it can be processed by optical signal processing circuits, such SiP filters [32] and phased-arrays [63], and then transported over long distances on a single-mode optical fiber. Here, we can safely assume that the optical device/channel is passive and noiseless. However, on-chip or in-package optical gain using a semiconductor optical amplifier (SOA) or erbium-doped fiber amplifier (EDFA) is also possible with the associated noise figure [64]. The optical channel power gain is given as $G_{ch} \triangleq \frac{P_{o,d}}{P_{M,o}} = \frac{1}{L_{ch}}$, where L_{ch} is the optical power loss. The detector is either interfaced with a passive load R_L, or a transimpedance amplifier (TIA). In this work, only passive load is considered. The detected power in the load is $P_L = i_d^2 R_L = (r_d \cdot P_{o,d})^2 R_L$ and thus detector gain is [36]

$$G_{det} \triangleq \frac{P_L}{p_{o,d}^2} = \frac{(r_d P_{o,d})^2 R_L}{P_{o,d}^2} = r_d^2 R_L \tag{45}$$

where r_d is the detector responsivity.

VI-2.2) RAMZM Link Gain: In section III, we developed the gain of RAMZM. To be able to find the gain of the entire link, the product of modulator and detector gain must be evaluated. For simplicity, it is assumed that there is no optical loss/gain element ($\frac{p_{o,d}^2}{P_{M,o}^2} = 1$) between modulator & detector and $R_s = R_L$. Therefore, the entire link gain can be expressed as-

$$G = \frac{P_{M,o}^2}{P_{s,a}} \cdot \frac{p_{o,d}^2}{P_{M,o}^2} \cdot \frac{P_L}{p_{o,d}^2} = \Big[\frac{\pi\gamma_1 P_I R_s r_d}{V_\pi L}\Big]^2 \tag{46}$$

Fig. 37(a) shows the contour plot for the RAMZM link gain, G, for various bias conditions (θ_{DC}, τ). As described in the previous section, the link gain is the highest when the thermal phase shifters on the RAMZM arm are tuned in such way that $\theta_{DC} = 0$.

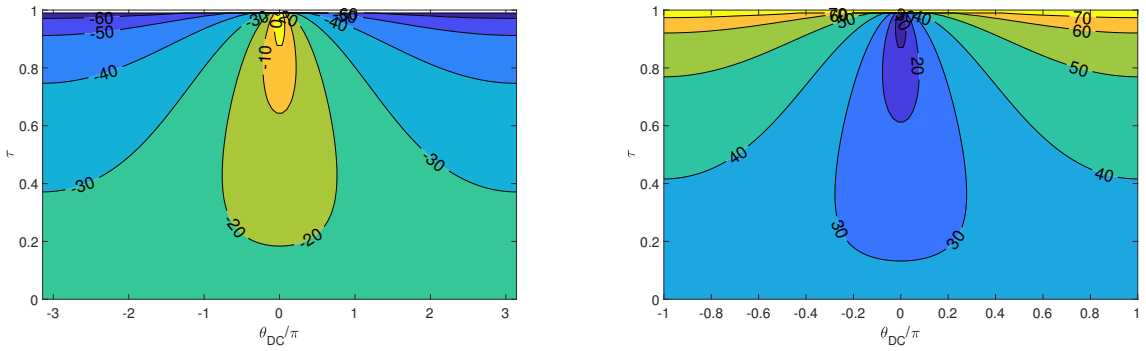

Figure 37: (a) RAMZM-based analog optical link Gain at different bias conditions (θ_{DC}, τ) while keeping $\phi_{bias} = \frac{\pi}{2}$. (b) NF at different bias conditions (θ_{DC}, τ) while keeping $\phi_{bias} = \frac{\pi}{2}$. The link parameters employed are listed in Table 6.

VI-2.3) RAMZM Link Noise Figure and Ring Biasing: The NF of the link is expressed as [36]

$$NF = 10 \cdot log_{10}\Big[1 + \frac{R_L}{4kTG}\Big(\frac{\overline{I_D}^2}{2} 10^{\frac{RIN}{10}} + 2q\overline{I_D}\Big) + \frac{1}{G}\Big] \tag{47}$$

where, RIN of the laser source is expressed in dB/Hz and the resulting RIN noise current spectral density (CSD) is given by $\overline{i_{RIN}^2} = \frac{\overline{I_D}^2}{2} 10^{\frac{RIN}{10}}$ where $\overline{I_D} = r_d P_{av} = \frac{r_d P_I}{2L}[1 + cos(\phi_{bias})]$ is average detector current [36]. $P_{av} = \frac{P_I}{2L}[1 + cos(\phi_{bias})]$ comes from Eq. 25, weighted by optical loss L. The detector shot noise current spectral density is described as $\overline{i_{sn}^2} = 2q\overline{I_D}$. Thus, RIN and shot noise CSD depend upon $\overline{I_D^2}$ and $\overline{I_D}$ respectively. The corresponding plot of NF for the different bias conditions (θ_{DC}, τ) is illustrated in Fig. 37(b). Here, it is evident that for $\theta_{DC} = 0$, NF is maximized due to the large link gain.

Fig. 38 (left) plots Eq. 47 with respect to the small-signal power gain, G. If the detector noise terms are ignored, then for large optical attenuation (i.e. $G \ll 0\ dB$), the load thermal noise dominates the detector noise terms and Eq. 47 reduces to the *passive attenuation limit* $NF = log_{10}\Big(1 + \frac{1}{G}\Big)$. For $G \gg 0\ dB$, the NF asymptotically approaches the *lossless match limit* of 0 dB. One can observe that the link NF is rather high due to the detector noise, as $\overline{I_D}$ depends upon $\frac{P_I}{2L}[1 + cos(\phi_{bias})]$. This can be improved by biasing the arms of the modulator at different angle, $\phi_{bias} > \frac{\pi}{2}$ [36,54], or by filtering out the optical carrier [54,65] using an on-chip SiP filter [2].

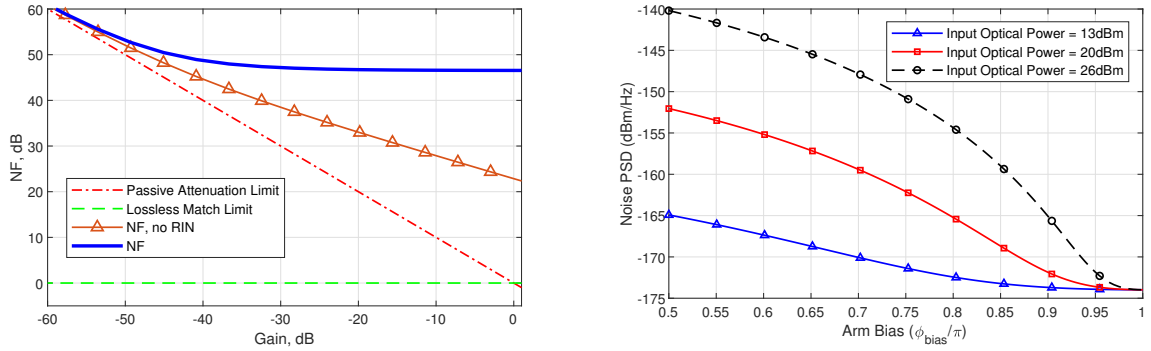

Figure 38: (left) NF versus gain for a RAMZM-based analog optical link. Here, P_I and L_{ch} are varied to sweep the gain. (right) RAMZM Noise PSD vs arm bias angle (ϕ_{bias}) for different input optical power, P_I.

As discussed before, the slope efficiency of RAMZM, when perfect third-order nonlinearity cancellation is achieved, is $\frac{1}{3}$ (or 9.54 dB lower power gain) compared to the MZMs (push-pull drive). This lower gain also result in higher NF in RAMZM, approximately by the same proportion. On the other hand, the gain enhanced RAMZM will have 9.54 dB improvements in both power gain and NF.

VI-2.4) Null Biasing of RAMZM: The RIN and shot noise CSD depend upon $\overline{I_D^2}$ and $\overline{I_D}$ respectively. This means, reducing $\overline{I_D}$ improves noise performance of the link, especially when the link is RIN limited ($\overline{I_D^2}$ dependence). Since $\overline{I_D} = \frac{r_d P_I}{2L}[1 + cos(\phi_{bias})]$, by changing ϕ_{bias} (null or low biasing [66,67]) we can reduce the overall noise as shown in Fig. 38 (right). Although the link gain reduces along with noise in null biasing technique (also known as low-biasing in the context of MZMs), the overall advantage in NF can be achieved, especially when a high laser power (P_I) is used as illustrated in Fig. 39.

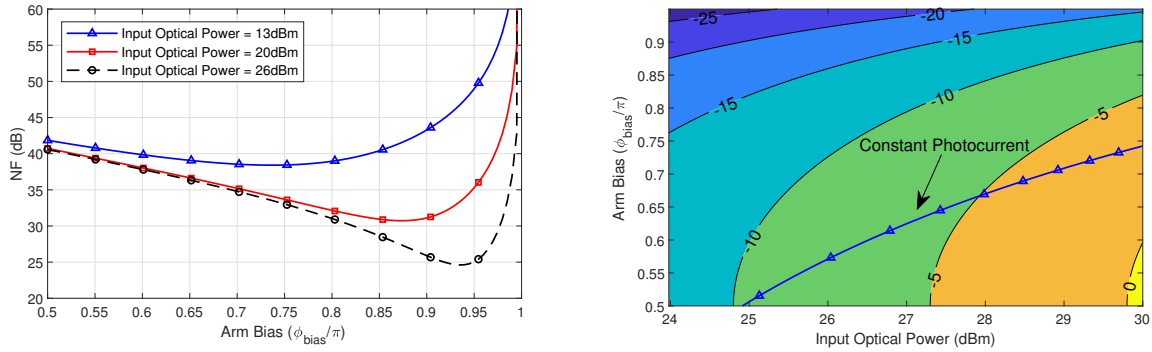

Figure 39: (left) RAMZM NF vs arm bias angle (ϕ_{bias}) for different input optical power. (right) Link Gain for various arm bias (ϕ_{bias}) and input optical power.

On the other hand, although mode evolution based photodiodes (PDs) provide higher saturation power over butt-coupled PDs [68], the use of high optical input power in integrated photonics is still limited due to poor saturation power performances of the PDs. In such cases, null biasing can be implemented in the RAMZM based analog optical link. When the link gain is limited by PD saturation, by employing null biasing one can increase the link gain without increasing PD current just by increasing the laser power (as shown in Fig. 39 (left)). In Fig. 39 (right), a constant photocurrent of 15.5mA [68] is plotted over the input laser power and RAMZM arm bias versus

Gain. It can be observed that by increasing laser power from 25 to 30dBm, it's possible to achieve a Link Gain advantage of >6dB when RAMZM arm bias is adjusted without having to increase the PD current.

VI-2.5) RAMZM Link Distortion Analysis: Fig. 36 had two active components that contribute distortion in the RF photonic link, namely the modulator and the detector. Unlike RAMZM, detector distortion does not arise from the optical to photo-current transfer characteristics, but from the higher-order effects [36]. These experimentally characterized effects depend upon the reverse bias voltage, $V_{b,pd}$, and $\overline{I_D}$, and can be minimized by using a sufficiently large $V_{b,pd}$ and avoiding detector saturation (by restricting $\overline{I_D}$ using null biasing technique) [36]. Since the distortion in an analog photonic link is dominated by the modulator nonlinearity, expressions for RAMZM IIP_3 and IIP_2 shown earlier in Section II and given by Eqs. 40-41 set the overall linearity for the RF photonic link.

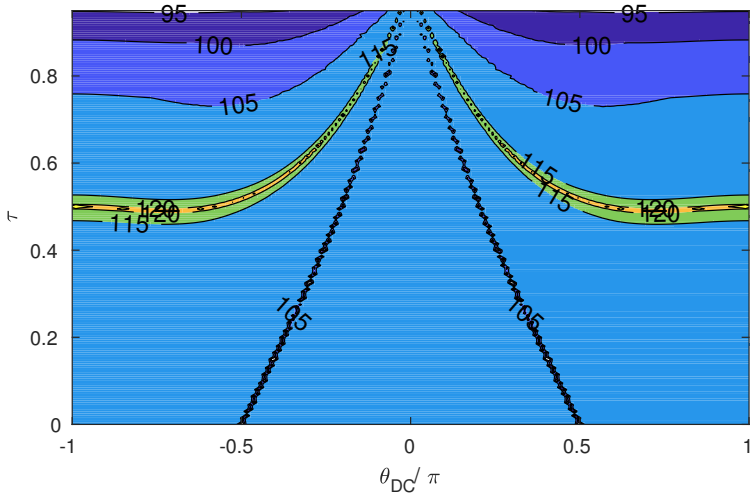

Figure 40: RAMZM-based analog optical link SFDR in $dB/Hz^{\frac{2}{3}}$ at different bias conditions, keeping $\phi_{bias} = \frac{\pi}{2}$.

To provide a comprehensive view of the link gain and total noise, SFDR is evaluated and plotted in Fig. 40 using the method described in [69] and link parameters listed in Table 6. Here, we see that the highest SFDR of ~ 128 $\text{dB/Hz}^{2/3}$ is obtained when the rings are biased in anti-resonance and $\tau = \frac{1}{2}$. As ring bias are tuned away from anti-resonance, a narrow band for coupling ratio τ exists for highest SFDR. The generated contours in Figs. 37 and 40 can be used together to make design trade-offs between the link NF and distortion.

VI-2.6) Linearity of Gain Enhanced (GE) RAMZM: In section III, we proposed a new biasing scheme where slope efficiency of RAMZM is upto 6× higher than that of MZMs. However, as previously discussed, this gain enhancement comes at the expense of linearity since θ_{DC} has to be shifted from π towards 0. In Fig. 41, we show that the SFDR of GE RAMZM is about 109.57 $dB/Hz^{\frac{2}{3}}$ at 1GHz. It is interesting to note that the GE RAMZM provides upto 6× improvement in slope efficiency over MZM while still providing the same SFDR performance as an MZM.

Analog optical link based on RAMZM was analyzed and compared with MZM-based links. We showed that the linearized RAMZM-based link provides $18\text{dB/Hz}^{\frac{2}{3}}$ or higher SFDR than its MZM counterpart. Furthermore, the tunable RAMZM that we fabricated, provides a trade-off space between the link Gain, Noise, Linearity performances based upon the rings' optical biasing.

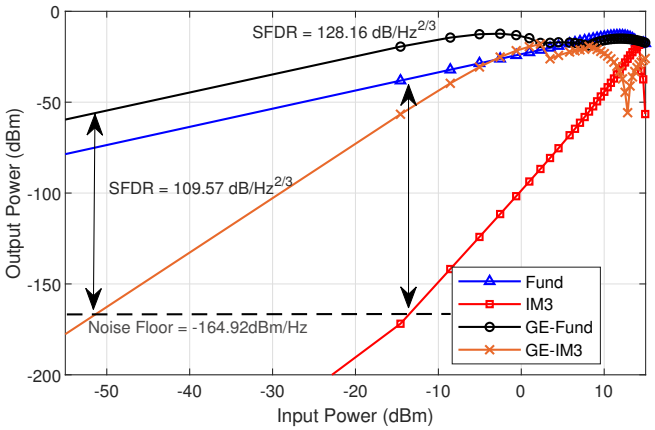

Figure 41: Comparison of SFDR performance of RAMZMs in a Photonic Link with different bias conditions. Here, Linearized and Gain Enhanced (GE) RAMZM bias conditions are $\{\phi_{bias}, \theta_{DC}, \tau\} = \{\frac{\pi}{2}, \pi, \frac{1}{2}\}$ and $\{\frac{\pi}{2}, 0, \frac{1}{2}\}$, respectively. Also, the link parameters are from Table 6.

VI-3. Ongoing and Future Experiments

Experimental characterization of complex PICs, such as the one designed in this project, require complex electronic backend infrastructure for tuning of PICs and applying RF inputs. A hardware prototyping platform was developed to test the designed PICs with nearly 300 electrical pads. First, a high-speed PC board was designed, then a packaging scheme was developed and accomplished through a commercial vendor (QP Technologies). Some of the experimental results are presented in this report along with the list of publications. Remaining experimental work includes: (i) Two-tone intermodulation distortion characterization of RAMZM using a 50GHz VNA at 1GH and 10GHz center frequencies, (ii) development of better filter tuning algorithms that are tolerant to thermal crosstalk by employing adaptive tuning and demonstration of experimental response that is close to the simulated response, (iii) Packaging and experimental characterization of the fabricated 2D mesh and experimental demonstration of the results obtained through simulation, and (iv) RF front-end demonstration by combining the components developed in the project.The results will be published in conference and journal papers.

VII. Conclusion and Broader Impacts of the Project

In this project, we demonstrated several large-scale integration of photonic integrated circuits, similar to electronic ICs. First, a full design and simulation flow and compact models were developed that enables optoelectronic IC designers to perform hybrid electronic-photonic cosimulation. Then, these developed models were used to first linearize a Mach-Zehnder modulator using an optical-domain ring-based approach that has several advantages over electronic-domain linearization. We also developed fully flexible and tunable optical filters capable of filtering RF signals and then also explored 2D mesh-based fully-flexible filter paradigm. While several results have been published, several more results will be available after ongoing experimental characterization.

In terms of impact, low-cost and small form-factor silicon-based RF and millimeter-wave photonic receiver components developed using project can potentially transform the U.S. wireless and semiconductor industry by enabling 6G wireless system by enabling targeted Tbps data rates. The flexible and frequency-agile receiver, resulting from the culmination of this work, will enable a warfighter to sift through several disparate RF and microwave bands and provide strategic superiority. Further, high dynamic range analog RF/mmWave photonic links can lead to novel massive-MIMO beamforming architectures that will enhance access to wireless spectrum in the

emerging available bands in the regions of spectrum in 5G and 6G standards, leading to metropolitan and rural wireless networks to bridge the digital divide across a wider population than today. We leveraged the Advanced Institute for Manufacturing for Integrated Photonics (AIM Photonics) established by DoD to design and demonstrate our prototypes, which can be used as examples by the scientists and researchers in the DOD and AFRL research labs.

References

[1] J. Shawon, Md. and V. Saxena, "Rapid Simulation of Photonic Integrated Circuits using Verilog-A Compact Models," in *IEEE Int. Midwest Symposium on Circuits and Systems (MWSCAS)*, Dallas, TX, 2019.

[2] M. J. Shawon and V. Saxena, "Rapid Simulation of Photonic Integrated Circuits Using Verilog-A Compact Models," *IEEE Transactions on Circuits and Systems I: Regular Papers*, pp. 1–11, 2020.

[3] "AIM Photonics Process Design Kits (PDKs)." [Online]. Available: http://www.aimphotonics.com/pdk/

[4] L. Chrostowski and M. Hochberg, *Silicon Photonics Design: From Devices to Systems*. Cambridge University Press, 2015.

[5] M. Hochberg, N. C. Harris, R. Ding, Y. Zhang, A. Novack, Z. Xuan, and T. Baehr-Jones, "silicon Photonics: The Next Fabless Semiconductor Industry," *IEEE Solid-State Circuits Magazine*, vol. 5, no. 1, pp. 48–58, 2013.

[6] T. Baehr-Jones, R. Ding, A. Ayazi, T. Pinguet, M. Streshinsky, N. Harris, J. Li, L. He, M. Gould, Y. Zhang, A. Eu-Jin, T.-Y. Liow, S. Hwee-Gee, G.-Q.-Q. Lo, and M. Hochberg, "A 25 Gb/s Silicon Photonics Platform," *arXiv preprint arXiv:1203.0767*, 2012. [Online]. Available: http://arxiv.org/abs/1203.0767

[7] P. Dumon, W. Bogaerts, R. Baets, J.-M. Fedeli, and L. Fulbert, "Towards foundry approach for silicon photonics: silicon photonics platform ePIXfab," *Electronics letters*, vol. 45, no. 12, pp. 581–582, 2009.

[8] "IMEC Silicon Photonics iSiPP50G." [Online]. Available: http://europractice-ic.com/mpw-prototyping/siphotonics/imec/

[9] A. Khanna, Y. Chen, A. Novack, Y. Liu, R. Ding, T. Baehr-Jones, and M. Hochberg, "Complexity scaling in silicon photonics," in *Optical Fiber Communication Conference*. Optical Society of America, 2017, pp. Th1B–3.

[10] G. Choo, S. Cai, B. Wang, C. K. Madsen, K. Entesari, and S. Palermo, "Automatic monitor-based tuning of reconfigurable silicon photonic apf-based pole/zero filters," *Journal of Lightwave Technology*, vol. 36, no. 10, pp. 1899–1911, 2018.

[11] J. Shawon, Md., R. Wang, and V. Saxena, "Design and Modeling of Silicon Photonic Ring-Based Linearized RF-to-Optical Modulator," in *in the proceedings of IEEE Int. Midwest Symposium on Circuits and Systems (MWSCAS)*, 2018.

[12] A. Jain, N. Hosseinzadeh, X. Wu, H. K. Tsang, R. Helkey, J. E. Bowers, and J. F. Buckwalter, "A high spur-free dynamic range silicon dc kerr ring modulator for rf applications," *Journal of Lightwave Technology*, vol. 37, no. 13, pp. 3261–3272, 2019.

[13] R. Helkey, A. A. Saleh, J. Buckwalter, and J. E. Bowers, "High-performance photonic integrated circuits on silicon," *IEEE Journal of Selected Topics in Quantum Electronics*, vol. 25, no. 5, pp. 1–15, 2019.

[14] FDTD Solutions 8.9, Lumerical Inc. [Online]. Available: https://www.lumerical.com/tcad-products/fdtd/

[15] W. Bogaerts and P. Dumon, "IPKISS Design Framework." [Online]. Available: http://www.ipkiss.org/

[16] M. Köfferlein, "Klayout," 2018.

[17] M. J. Shawon and V. Saxena, "Rapid simulation of photonic integrated circuits using verilog-a compact models," in *2019 IEEE 62nd International Midwest Symposium on Circuits and Systems (MWSCAS)*. IEEE, 2019, pp. 424–427.

[18] C. Sorace-Agaskar, J. Leu, M. R. Watts, and V. Stojanovic, "Electro-optical co-simulation for integrated cmos photonic circuits with verilоga," *Optics express*, vol. 23, no. 21, pp. 27 180–27 203, 2015.

[19] C. M. Sorace-Agaskar, "Analog integrated photonics," Ph.D. dissertation, Massachusetts Institute Of Technology, 2015.

[20] J. Cioffi, *Signal Processing and Detection*. Stanford University. [Online]. Available: https://web.stanford.edu/group/cioffi/doc/book/

[21] E. Kononov, "Modeling photonic links in verilog-a," Ph.D. dissertation, Massachusetts Institute of Technology, 2013.

[22] X.-G. Xia, "System identification using chirp signals and time-variant filters in the joint time-frequency domain," *IEEE Transactions on Signal Processing*, vol. 45, no. 8, pp. 2072–2084, 1997.

[23] S. Qian and D. Chen, "Joint time-frequency analysis," *IEEE Signal Processing Magazine*, vol. 16, no. 2, pp. 52–67, 1999.

[24] I. H. Chan, "Swept sine chirps for measuring impulse response [j]," *Power (dBVrms)*, vol. 50, no. 40, p. 30, 2010.

[25] T. Paavle, M. Min, and T. Parve, "Aspects of using chirp excitation for estimation of bioimpedance spectrum," in *Fourier Transform-Signal Processing*. IntechOpen, 2012.

[26] C. Cook and M. Bernfeld, *Radar Signals: An Introduction to Theory and Application*. Academic Press, 1967.

[27] "Chirp spectrum." [Online]. Available: https://web.archive.org/web/20191111030920/https://en.wikipedia.org/wiki/Chirp_spectrum

[28] INTERCONNECT 4.1, Lumerical Inc. [Online]. Available: https://www.lumerical.com/tcad-products/interconnect/

[29] P. A. Regalia, S. K. Mitra, and P. Vaidyanathan, "The digital all-pass filter: A versatile signal processing building block," *Proceedings of the IEEE*, vol. 76, no. 1, pp. 19–37, 1988.

[30] C. Madsen, "Efficient architectures for exactly realizing optical filters with optimum bandpass designs," *Photonics Technology Letters, IEEE*, vol. 10, no. 8, pp. 1136–1138, 1998.

[31] C. K. Madsen and J. H. Zhao, *Optical Filter Design and Analysis*. Wiley-Interscience, 1999.

[32] G. Choo, S. Cai, B. Wang, C. K. Madsen, K. Entesari, and S. Palermo, "Automatic monitor-based tuning of reconfigurable silicon photonic apf-based pole/zero filters," *Journal of Lightwave Technology*, vol. 36, no. 10, pp. 1899–1911, 2018.

[33] J. Rhim, Y. Ban, B.-M. Yu, J.-M. Lee, and W.-Y. Choi, "Verilog-a behavioral model for resonance-modulated silicon micro-ring modulator," *Optics express*, vol. 23, no. 7, pp. 8762–8772, 2015.

[34] L. Zhang, Y. Li, J.-Y. Yang, M. Song, R. G. Beausoleil, and A. E. Willner, "Silicon-based microring resonator modulators for intensity modulation," *IEEE Journal of Selected Topics in Quantum Electronics*, vol. 16, no. 1, pp. 149–158, 2009.

[35] B. E. Little, S. T. Chu, H. A. Haus, J. Foresi, and J.-P. Laine, "Microring resonator channel dropping filters," *Journal of lightwave technology*, vol. 15, no. 6, pp. 998–1005, 1997.

[36] C. H. Cox, *Analog optical links: theory and practice*. Cambridge University Press, 2006.

[37] V. J. Urick, K. J. Williams, and J. D. McKinney, *Fundamentals of microwave photonics*. John Wiley & Sons, 2015.

[38] N. Hosseinzadeh, A. Jain, R. Helkey, and J. F. Buckwalter, "A distributed low-noise amplifier for broadband linearization of a silicon photonic mach-zehnder modulator," *IEEE Journal of Solid-State Circuits*, 2020.

[39] B. Analui, A. Rylyakov, S. Rylov, M. Meghelli, and A. Hajimiri, "A 10-Gb/s Two-dimensional Eye-opening Monitor In 0.13-μm Standard CMOS," *IEEE Journal of Solid-State Circuits*, vol. 40, no. 12, pp. 2689–2699, 2005.

[40] K. Zhu, V. Saxena, X. Wu, and W. Kuang, "Design considerations for traveling-wave modulator-based cmos photonic transmitters," *IEEE Transactions on Circuits and Systems II: Express Briefs*, vol. 62, no. 4, pp. 412–416, 2015.

[41] C. G. Bottenfield, V. A. Thomas, and S. E. Ralph, "Silicon photonic modulator linearity and optimization for microwave photonic links," *IEEE Journal of Selected Topics in Quantum Electronics*, vol. 25, no. 5, pp. 1–10, 2019.

[42] E. Timurdogan, C. V. Poulton, M. Byrd, and M. Watts, "Electric field-induced second-order nonlinear optical effects in silicon waveguides," *Nature Photonics*, vol. 11, no. 3, pp. 200–206, 2017.

[43] R. Sadhwani and B. Jalali, "Adaptive cmos predistortion linearizer for fiber-optic links," *Journal of Lightwave Technology*, vol. 21, no. 12, p. 3180, 2003.

[44] J. Okyere, K. Yu, K. Entesari, and S. Palermo, "A fifth-order polynomial predistortion circuit for mach-zehnder modulator linearization in 65nm cmos," in *2017 Texas Symposium on Wireless and Microwave Circuits and Systems (WMCS)*. IEEE, 2017, pp. 1–4.

[45] C. Li, K. Yu, J. Rhim, K. Zhu, N. Qi, V. Saxena, M. Fiorentino, and S. Palermo, "A 3D-Integrated 56 Gb/s NRZ/PAM4 Reconfigurable Segmented Mach-Zehnder Modulator based Si-photonics Transmitter," in *IEEE BiCMOS and Compound Semiconductor Integrated Circuits and Technology Symposium (BCICTS)*, 2018.

[46] R. Ding, Z. Xuan, P. Yao, D. Prather, M. Hochberg, and T. Baehr-Jones, "100-gb/s nrz optical transceiver analog front-end in 130-nm sige bicmos," in *2014 Optical Interconnects Conference*. IEEE, May 1959.

[47] H. Zhang and E. Sánchez-Sinencio, "Linearization techniques for cmos low noise amplifiers: A tutorial," *IEEE Transactions on Circuits and Systems I: Regular Papers*, vol. 58, no. 1, pp. 22–36, 2010.

[48] D. Zhu, J. Chen, and S. Pan, "Multi-octave linearized analog photonic link based on a polarization-multiplexing dual-parallel mach-zehnder modulator," *Optics express*, vol. 24, no. 10, pp. 11 009–11 016, 2016.

[49] A. Ayazi, T. Baehr-Jones, Y. Liu, A. E.-J. Lim, and M. Hochberg, "Linearity of silicon ring modulators for analog optical links," *Optics express*, vol. 20, no. 12, pp. 13 115–13 122, 2012.

[50] A. Gutierrez, A. Brimont, G. Rasigade, M. Ziebell, D. Marris-Morini, J.-M. Fedeli, L. Vivien, J. Marti, and P. Sanchis, "Ring-assisted Mach–Zehnder interferometer silicon modulator for enhanced performance," *Journal of Lightwave Technology*, vol. 30, no. 1, pp. 9–14, 2012.

[51] J. Cardenas, P. A. Morton, J. B. Khurgin, A. Griffith, C. B. Poitras, K. Preston, and M. Lipson, "Linearized silicon modulator based on a ring assisted Mach Zehnder inteferometer," *Optics express*, vol. 21, no. 19, pp. 22 549–22 557, 2013.

[52] P. A. Morton, J. Cardenas, M. Lipson, and J. B. Khurgin, "Morton photonics inc., west friendship, md 21794," in *Microwave Photonics (MWP), 2013 International Topical Meeting on*. IEEE, 2013, pp. 275–277.

[53] P. Yue, X. Yi, Q.-N. Li, T. Wang, and Z.-J. Liu, "Mmi-based ultra linear electro-optic modulator with high output rf gain," *Optik-International Journal for Light and Electron Optics*, vol. 124, no. 17, pp. 2623–2626, 2013.

[54] D. Marpaung, "High dynamic range analog photonic links design and implementation," *University of Twente*, 2009.

[55] H. Jayatilleka, K. Murray, M. Á. Guillén-Torres, M. Caverley, R. Hu, N. A. Jaeger, L. Chrostowski, and S. Shekhar, "Wavelength tuning and stabilization of microring-based filters using silicon in-resonator photoconductive heaters," *Optics express*, vol. 23, no. 19, pp. 25 084–25 097, 2015.

[56] C. Zhang, P. A. Morton, J. B. Khurgin, J. D. Peters, and J. E. Bowers, "Ultralinear heterogeneously integrated ring-assisted mach–zehnder interferometer modulator on silicon," *Optica*, vol. 3, no. 12, pp. 1483–1488, 2016.

[57] D. Pérez, I. Gasulla, L. Crudgington, D. J. Thomson, A. Z. Khokhar, K. Li, W. Cao, G. Z. Mashanovich, and J. Capmany, "Multipurpose silicon photonics signal processor core," *Nature communications*, vol. 8, no. 1, p. 636, 2017.

[58] L. Zhuang, C. G. Roeloffzen, M. Hoekman, K.-J. Boller, and A. J. Lowery, "Programmable photonic signal processor chip for radiofrequency applications," *Optica*, vol. 2, no. 10, pp. 854–859, 2015.

[59] M. Bahadori, A. Gazman, N. Janosik, S. Rumley, Z. Zhu, R. Polster, Q. Cheng, and K. Bergman, "Thermal rectification of integrated microheaters for microring resonators in silicon photonics platform," *Journal of Lightwave Technology*, vol. 36, no. 3, pp. 773–788, 2017.

[60] M. J. Shawon and V. Saxena, "Analysis of Trade-offs in RF Photonic Links based on Multi-Bias Tuning of Silicon Photonic Ring-Assisted Mach Zehnder Modulators," *under review in the IEEE Transactions on Circuits and Systems I: Regular Papers*, 2021.

[61] M. Liao, S. Chen, Z. Liu, Y. Wang, L. Ponnampalam, Z. Zhou, J. Wu, M. Tang, S. Shutts, Z. Liu *et al.*, "Low-noise 1.3 μm inas/gaas quantum dot laser monolithically grown on silicon," *Photonics Research*, vol. 6, no. 11, pp. 1062–1066, 2018.

[62] E. Timurdogan, Z. Su, R.-J. Shiue, C. V. Poulton, M. J. Byrd, S. Xin, and M. R. Watts, "Apsuny process design kit (pdkv3. 0): O, c and l band silicon photonics component libraries on 300mm wafers," in *2019 Optical Fiber Communications Conference and Exhibition (OFC)*. IEEE, 2019, pp. 1–3.

[63] G. Choo, C. K. Madsen, S. Palermo, and K. Entesari, "Automatic monitor-based tuning of an rf silicon photonic 1x4 asymmetric binary tree true-time-delay beamforming network," *Journal of Lightwave Technology*, vol. 36, no. 22, pp. 5263–5275, 2018.

[64] T. Matsumoto, T. Kurahashi, R. Konoike, K. Suzuki, K. Tanizawa, A. Uetake, K. Takabayashi, K. Ikeda, H. Kawashima, S. Akiyama *et al.*, "Hybrid-integration of soa on silicon photonics platform based on flip-chip bonding," *Journal of Lightwave Technology*, vol. 37, no. 2, pp. 307–313, 2018.

[65] M. LaGasse, W. Charczenko, M. Hamilton, and S. Thaniyavarn, "Optical carrier filtering for high dynamic range fibre optic links," *Electronics Letters*, vol. 30, no. 25, pp. 2157–2158, 1994.

[66] M. L. Farwell, W. S. Chang, and D. R. Huber, "Increased linear dynamic range by low biasing the mach-zehnder modulator," *IEEE Photonics Technology Letters*, vol. 5, no. 7, pp. 779–782, 1993.

[67] M. M. Sisto, S. LaRochelle, and L. A. Rusch, "Gain optimization by modulator-bias control in radio-over-fiber links," *Journal of lightwave technology*, vol. 24, no. 12, pp. 4974–4982, 2006.

[68] M. J. Byrd, E. Timurdogan, Z. Su, C. V. Poulton, N. M. Fahrenkopf, G. Leake, D. D. Coolbaugh, and M. R. Watts, "Mode-evolution-based coupler for high saturation power ge-on-si photodetectors," *Optics letters*, vol. 42, no. 4, pp. 851–854, 2017.

[69] K. Kundert, "Accurate and rapid measurement of ip2 and ip3," *The Designers Guide Community, www. designersguide. org/Analysis/intercept-point. pdf*, 2002.